Development of novel 2D and 3D correlative microscopy to characterise the composition and multiscale structure of suspended sediment aggregates.

Jonathan A.T. Wheatland [a,b,c], Kate L. Spencer [c], Ian G. Droppo [d], Simon J. Carr [c,e] Andrew J. Bushby[a,b,*]

[a] School of Engineering & Materials Science, Queen Mary University of London, Mile End Road, London E1 4NS, UK

[b] The NanoVision Centre, Queen Mary University of London, Mile End Road, London E1 4NS, UK

[c] School of Geography, Queen Mary University of London, Mile End Road, London E1 4NS, UK

[d] Environment and Climate Change Canada, 867 Lakehouse Road, P.O. Box 5050, Burlington, Ontario L7S 1A1, Canada

[e] Department of Science, Natural Resources and Outdoor Studies, University of Cumbria, Ambleside, Cumbria LA22 8BB, UK

* Corresponding author. Email address: a.j.bushby@qmul.ac.uk

Abstract

Suspended cohesive sediments form aggregates or ‘flocs’ and are often closely associated with carbon, nutrients, pathogens and pollutants, which makes understanding their composition, transport and fate highly desirable. Accurate prediction of floc behaviour requires the quantification of 3-dimensional (3D) properties (size, shape and internal structure) that span several scales (i.e. nanometre [nm] to millimetre [mm]-scale). Traditional techniques (optical cameras and electron microscopy [EM]), however, can only provide 2-dimensional (2D)

simplifications of 3D floc geometries. Additionally, the existence of a resolution gap between conventional optical microscopy (COM) and transmission EM (TEM) prevents an understanding of how floc nm-scale constituents and internal structure influence mm-scale floc properties. Here, we develop a novel correlative imaging workflow combining 3D X-ray micro-computed tomography (µCT), 3D focused ion beam nanotomography (FIB-nt) and 2D scanning EM (SEM) and TEM (STEM) which allows us to stabilise, visualise and quantify the composition and multi-scale structure of sediment flocs for the first time. This new technique allowed the quantification of 3D floc geometries, the identification of individual floc components (e.g., clays, non-clay minerals and bacteria), and characterisation of particle-particle and structural associations across scales. This novel dataset demonstrates the truly complex structure of natural flocs at multiple scales. The integration of multi scale, state-of-the-art instrumentation/techniques offers the potential to generate fundamental new understanding of floc composition, structure and behaviour.

Keywords

Aquatic sediments, sediment aggregates, flocs, multiscale imaging, 2D and 3D correlative microscopy

1. Introduction

Cohesive fine-grained sediments and mixed sediments in suspension influence a wide array of environmental processes and material transfers, including the transport, fate and effect of carbon, nutrients, microbiota (including pathogens) and pollutants within lakes, rivers, estuaries and the marine environment (Azam & Long 2001; Rusconi et al. 2014; Rummel et al. 2017). Understanding the composition and behaviour of cohesive and mixed sediments is therefore a major issue for the

management of aquatic environments. However, in suspension this biotic and abiotic particulate matter forms loosely bound, complex and fragile aggregates, or ‘flocs’. Flocs exhibit hydrodynamics (e.g., transport dynamics and settling) that differ significantly from those of their constituent particles (Droppo 2001; Burd & Jackson 2009; Manning et al. 2010).

To predict the movement of cohesive sediments requires accurate quantification of floc properties that control their behaviour (e.g., size, shape, porosity and density) (Soulsby et al. 2013). Additionally, an understanding of floc composition and particle associations provides a mechanistic understanding of e.g., pathogen and pollutant transport and elucidates microbial dynamics (Liss 2002). Yet, obtaining such empirical data is challenging since flocs are inherently fragile and their properties often span several spatial scales, i.e. nm to mm-scale. Flocs are routinely characterised based on their ‘gross’ scale properties (e.g., external size and shape) that can be measured in situ relatively simply and non-destructively. Floc camera systems (e.g., LabSFLOC, Manning & Dyer 2002) and laser diffraction particle sizers (e.g., LISST, Agrawal & Pottsmith 2000) are commonly used and provide additional measurements of floc settling velocities. Internal floc characteristics (e.g., structure, density and porosity) cannot be measured directly using these methods, but can be estimated using Stokes’ Law and the assumption of spherical shape and fractal behaviour, i.e. structural self-similarity (Winterwerp 1998; Jarvis et al. 2005). Alternatively, sub-µm structures and the internal composition can be observed by, for instance, TEM (Leppard et al. 1996) or optical measurement of cell colonisation (e.g., Nguyen et al. 2017). However, there is no one method that allows floc structure and composition to be observed at all relevant spatial scales or that reflects the inherent 3D nature of these characteristics. A major challenge

therefore is the development of methods that enable empirical observation and accurate quantification of floc characteristics, correlated across multiple length-scales.

The combined application of two or more imaging methods, known as correlative microscopy, overcomes the resolution limitations associated with using a single imaging technique (Liss et al. 1996; Burnett et al. 2014). Previously, COM has been applied correlatively with confocal laser scanning microscopy (CLSM) and TEM enabling the investigation of floc mm-and nm-scale properties (Leppard 1992; Droppo et al. 1996; Liss et al. 1996; Leppard et al. 1996). Observations using this approach have provided valuable insights into floc structure-function relationships, highlighting the importance of floc-colonising microorganisms and their associated exopolymeric substances (EPS) (Droppo 2001; Tolhurst et al. 2002). However, the use of these imaging methods in a truly correlative manner is hindered by the specific preparation requirements, differences in contrast mechanisms, lack of overlap in resolution and their 2-dimensionality. Methods that can combine different spatial scales and similar contrast mechanisms with both 2D and 3D information are needed to understand delicate floc structures that include both organic and inorganic materials that extend across multiple scales. The combination of X-ray tomography with EM has the capability to achieve this across length-scales from mm to nm and the resolution gap can be closed. Furthermore, with similar sample preparation procedures, both imaging techniques can be applied to a single floc sample. Such methods have been used within materials science to visualise and quantify complex, multiscale structures from the cm to nm-scale (Handschuh et al. 2013; Burnett et al. 2014), and in the biological sciences (Bushby et al. 2012), but have not yet been applied to study natural environmental samples.

µCT and FIB-nt are both capable of imaging complex samples in 3D. µCT is capable of analysing volumes at a higher resolution than COM, and for small samples can reach a resolution of tens of µm down to submicrometre (Cnudde & Boone 2013). It is non-destructive and thus suited to imaging delicate samples, including sediments and hydrated, flocculated clays (e.g., Sharma et al. 2017; Zhang et al. 2018). FIB-nt is capable of resolutions approaching that of TEM (c. 10 nm, Holzer et al. 2004), and occupies a niche between TEM and µCT. Although FIB-nt is destructive, delicate samples can be stabilised to preserve their integrity during analysis (e.g., Bushby et al. 2011), and it has recently been successfully applied to investigate the internal structure of hydrated flocs (Wheatland et al. 2017). Significantly, both µCT and FIB-nt provide quantitative data (Holzer et al. 2004; Ketcham & Carlson 2001), which can be used to characterise suspended sediment flocs and potentially parameterise computational models that describe floc behaviour.

The aim of this study is to develop a correlative workflow that enables observation, characterisation and quantification of natural suspended sediment floc structure and composition from the mm to nm-scale for the first time. This workflow, which combines 3D µCT and FIB-nt with 2D SEM and STEM, is applied to the investigation of natural estuarine sediment flocs. Based on feature greyscale, size and morphology criteria are developed to distinguish floc components (e.g., clay minerals, bacteria etc.) observed at different spatial scales, which are used to segment the datasets.

2. Materials and Methods

2.1. Considerations for Correlative Imaging

Several challenges exist for the correlative imaging of sediment flocs. Firstly, fragile flocs must be sampled and stabilised and contrast agents (e.g., stains) applied to enable feature recognition using different imaging modalities operating at different scales (Wheatland et al. 2017). µCT and EM share similar contrast mechanisms allowing object(s) of interest to be identified and correlated between datasets. However, electron-dense stains must be introduced to allow organics to be distinguished. Secondly, to achieve correlation between the different imaging methods, datasets must be registered using fiducial markers that can be imaged by all methods. Thirdly, the process of identifying nm-scale datasets nested within mm-scale samples is represents a significant challenge (Bushby et al. 2011; Burnett et al. 2014). Therefore, workflows must follow a targeted approach whereby a sample is sequentially imaged at a finer scale and/or by a complimentary modality, the data from which is used to selected further regions of interest (RoI) for analysis at higher resolutions. Finally, the imaging methods used should each adequately resolve both the biotic and abiotic floc components for correlation. For example, µCT maps X-ray attenuation and hence images the density of an object or concentration of floc constituents at the µm to mm-scale. In comparison, SEM (using secondary and backscattered electrons) provides information on morphology and elemental composition at the nm to µm-scale. Combining this information enables important features (e.g., a pore space, clay mineral or bacteria) to be identified at different scales and resolutions. Once features have been identified, they can be segmented, quantified and visualised in both µCT and FIB-nt.

2.2. Floc Capture and Stabilisation

Natural sediment collected from the Thames Estuary, SE England. These sediments are typically fully saline, fine grained silty clays with organic content typically < 10% (measured as % loss on ignition, e.g., O'Shea et al. 2018). Sediment was added to an artificial seawater solution (Sigma sea salts 34 g L^{-1}) and gently agitated using a magnetic stirrer to induce flocculation. Fragile flocs were sampled following the protocol outlined in Droppo et al. (1996), which involved settling flocs directly into plankton chambers and immobilising flocs in agarose gel. µCT scans of a test sample (FS0, see Fig. S1 of Supplementary Materials) were conducted in order to assess potential artefacts associated with this technique (e.g., particle-particle overlap, Droppo et al. 1996). Immobilised flocs were subsequently prepared for imaging following the block staining protocol outlined in Wheatland et al. (2017). Floc samples were rendered vacuum stable by resin embedding, which included the addition of electron dense stains (e.g., uranyl acetate etc.) to improve the contrast of organic constituents. Following resin embedding, fiducial markers (aluminium wire, c. 0.5 mm diameter) were implanted in the base of each resin block for the purpose of data co-registration (see Section 2.3). Aluminium was selected as it could be easily distinguished from natural sedimentary material using all imaging methods (Handschuh et al. 2013).

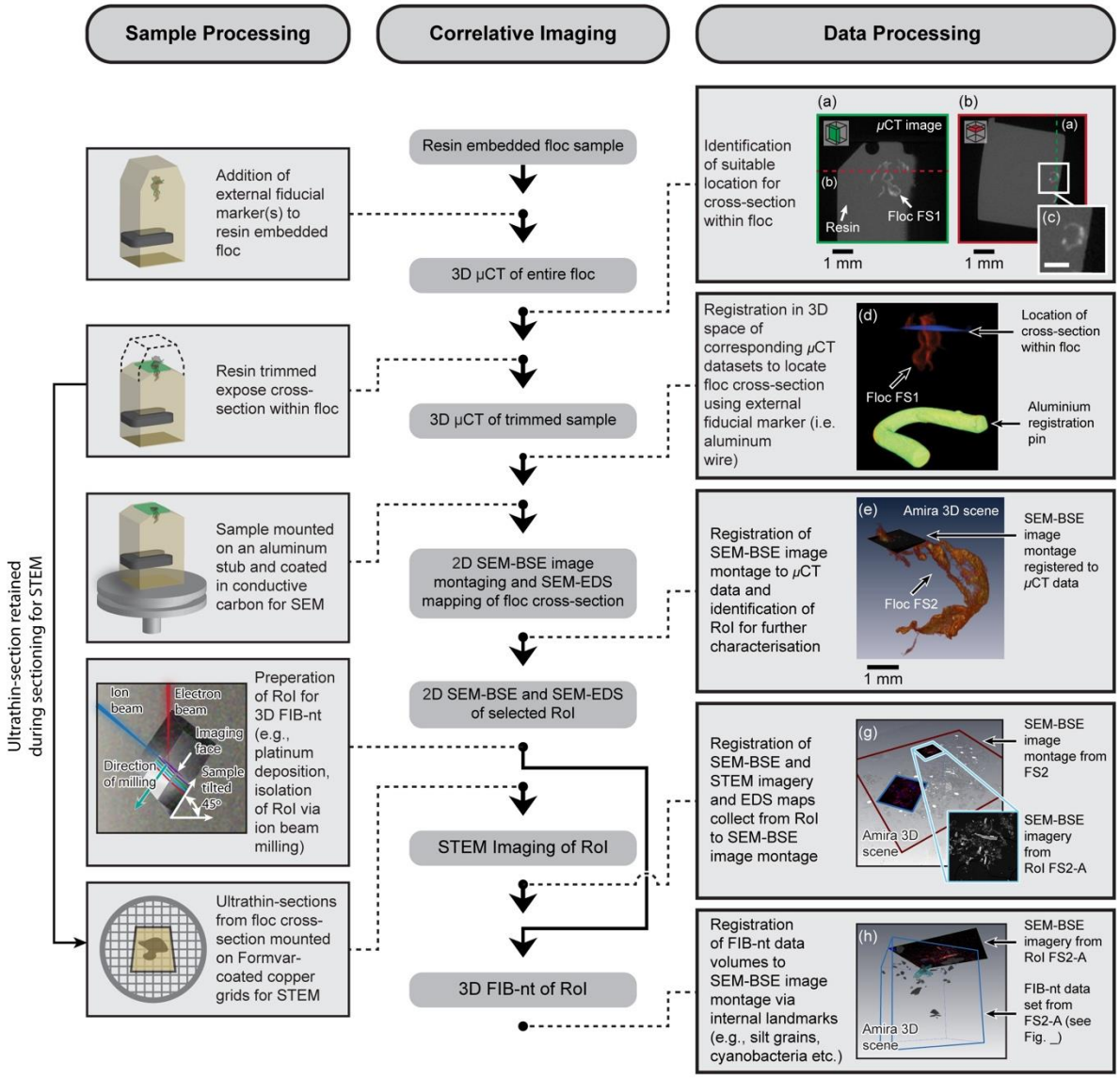

Figure 1. Flow diagram outlining the various stages in the correlative imaging workflow, including steps required for sample and data processing. Images (a) and (b) are orthogonal slices from the µCT scan of floc FS1. Grey-scale variations reflect regions of high and low X-ray attenuation (c), and indicate variability of floc constituents and structure at the sub-voxel scale. This information helps guide the selection of a suitable site for a cross-section within the floc which is exposed via ultramicrotomy. The precise location of the cross-section within the floc is then verified by re-scanning the sample using µCT and registering the two corresponding µCT datasets using the aluminium registration pin (d). 2D SEM-BSE image montages of the floc cross-section, obtained to identify suitable RoI for further analysis, are then registered to the µCT data (e). Following 2D SEM-BSE imaging, RoI are prepared for 3D FIB-nt (h). 2D SEM-BSE and STEM imagery and 3D FIB-nt data obtained from RoI can be registered to the image montage based on 'internal' fiducial markers (e.g., silt grains, cyanobacteria etc.) that can be identified in the corresponding datasets (g and h).

2.3. Description of the Correlative Workflow

The correlative workflow developed for investigating floc composition and multiscale structure is shown in Fig. 1. Low-resolution µCT scans (3D pixel or 'voxel' size, c. 10 μm^3) were initially conducted to characterise floc size and morphology and identify RoI for further analysis (Fig. 1a and b). At this resolution individual floc constituents <100 µm (e.g., bacteria and clay minerals) cannot be resolved. However, variations in X-ray attenuation (Fig. 1c and Fig. S2 of Supplementary Materials) indicate the variability of floc constituents and structure at the sub-voxel scale. Subsequently, selected RoIs were exposed by trimming the resin-block using an ultramicrotome (Leica UCT ultramicrotome), creating a smooth cross-section suitable for 2D SEM and 3D FIB-nt. During this process, ultrathin-sections (thickness, 70−100 nm) cut directly adjacent to the cross-section were retained for STEM (Fig. 1).

The accurate co-registration of µm and nm-scale EM datasets with mm-scale µCT scans relied on the location and characterisation of the cross-section created within the floc. Therefore, samples were re-scanned using µCT following ultramicrotomy to locate the floc cross-section within the original µCT data (Fig. 1d). This was facilitated by 'external' fiducial markers (aluminium wire) identifiable in the corresponding µCT datasets (Fig. 1d, see section 3.1.1). To ensure these repeat scans were directly comparable to the original µCT data and accurate co-registration, the position of the mechanical stage, manipulator settings (i.e. voltage and current) and resolution were kept constant.

2D SEM-BSE image montaging of the cross-section (block-face SEM) then provided the context within which to locate 3D FIB-nt volumes and 2D STEM imagery based on identification of 'internal' landmarks within the floc (Fig. 1g and h). Landmarks were selected that could be identified across scales and imaging

195 modalities, e.g., silt grains and cyanobacteria (see Table 1). Image montages were
196 obtained by systematic imaging using 2D SEM, resulting in 10's – 100's of images
197 that were stitched together to provide a 'panoramic' view of the entire cross-section
198 (pixel resolution, c. 100 nm^2). Following SEM imaging, elemental maps were
199 obtained from selected RoI via energy dispersive X-ray spectroscopy (SEM-EDS)
200 which, in conjunction with contrast and morphological information from SEM
201 imagery, enabled identification and mapping of materials.

202 2D SEM imagery and EDS maps informed the selection suitable sites for 3D
203 FIB-nt. Representativity is a key consideration when selecting parameters for FIB-nt
204 (i.e. volume size and resolution), and must be optimised to resolve features of
205 interest and ensure that a representative number of particles are characterised for
206 statistical analysis (Bushby et al. 2011). Natural flocs are compositionally complex,
207 containing particles of varying morphology and size (e.g., blocky silt grains, platy
208 clays, and filamentous organics), and high-resolution datasets are desirable (10-15
209 nm) to characterise individual particles. However, a trade-off must be made between
210 the resolution and volume size to ensure the µm-scale structures into which floc
211 constituents are organised are adequately characterised.

212

Imaging Technique; Successive Techniques Applied ⟶							
CT Datasets		SEM-BSE Montaging		SEM and STEM		FIB-nt	
Material	Identification Criteria	Material	Identification Criteria	Material	Identification Criteria	Material	Identification Criteria
Floc	Mid-range greyscale (c. 19,000 – 40,000) Variability in composition and structure at the sub-voxel scale	*Floc Matrix*	Material with diameter c. <10 µm, low to mid-range greyscales (c. 20 – 200) Regions of low and high occupation	*Clay Minerals*	2D planar morphology, size c. <5 µm, mid-range greyscale (c. 10 - 170)	*Clay minerals*	3D planar morphology, size c. <5 µm, mid-range greyscale (c. 10 - 170)
				Microbial Cells	Small size (c. <10 µm), high greyscale (c. 200 - 250),	*Cell Morpho-type*	Five cell morphotypes recognised based on

	recognised based on X-ray attenuation: low greyscale values (c. 25,000 – 40,000) correlated to regions of low-occupation, high greyscale values (c. 19,000 – 25,000) correlated to regions of high-occupation		identified based on greyscale, e.g., low occupation c. <50, high occupation c. >70		differential staining of subcellular structures		criteria outlined in Dazzo & Niccum (2015) (see Fig. 5)
						Intra-cellular Integrity	Three categories of intracellular integrity (indicative of metabolic state) recognised based on criteria outlined by Heissenberger et al. (1996) (see Fig. 5)
				Organo-Mineral Debris	Geometric structure, mid-range greyscale (c. 10 - 170)	*Organo-Mineral Debris*	Geometric structure, mid-range greyscale (c. 10 - 170)
				EPS	Fibrillar material, diameter (2 – 15 nm)	NA	
		Non-Clay Minerals	Blocky/ irregular morphology, particle size c. 5 – 40 µm, mid-range greyscales (c. 20 – 100)	*Non-Clay Minerals*	Blocky/ irregular morphology Particle size c. 5 – 40 µm, mid-range greyscales (c. 20 – 100)	*Non-Clay Minerals*	Blocky/ irregular morphology Particle size c. 5 – 40 µm, mid-range greyscales (c. 20 – 100)
		Bio-Organic Material	Irregularly shaped, high greyscales (c. 200 – 255)	*Bio-Organic Material*	Irregularly shaped, high greyscales (c. 200 – 255)	*Bio-Organic Material*	Irregularly shaped, high greyscales (c. 200 – 255)
Resin	Low greyscale (c. 7,000 – 17,000)	*Resin External to the Floc*	Resin external to the floc matrix, grey-scale (c. 0 – 20)	*Resin External to the Floc*	0 – 20	NA	
		Resin Filled Pore-Space	Resin filled pores within the floc matrix, low grey-scale (c. 0 – 20). NB only possible to resolve pores with diameter >30 µm	µm-Scale Pore	Resin filled pores within the floc matrix, low grey-scale (c. 0 – 20), diameter <10 µm	µm-Scale Pore	Resin filled pores within the floc matrix, low grey-scale (c. 0 – 20), diameter <10 µm
				nm-Scale Pores	Resin filled pores within the floc matrix, low grey-scale (c. 0 – 20), diameter >10 µm	nm-Scale Pores	Resin filled pores within the floc matrix, low grey-scale (c. 0 – 20), diameter >10 µm

Aluminium Pin	High greyscale (c. 45,000 – 65,535)	NA

Table 1. Materials identified within the various 2D and 3D datasets, and the criteria used for their identification/segmentation, e.g., size, morphology, and greyscale characteristics. Note, that the µCT are 16-bit and therefore have a pixel depth of 65,535 greyscales, whereas the SEM and STEM imagery and FIB-nt data volumes are 8-bit with a 256 greyscale range.

Ultrathin-sections collected adjacent to the surface of the cross-section during ultramicrotomy were mounted on Formvar-covered copper grids (Gilder Grids) and coated in conductive carbon for STEM. STEM provided details of the pore space that cannot be obtained using SEM. Additionally, high-resolution elemental analysis via STEM X-ray spectroscopy (STEM-EDS) conducted on floc cross-section (SEM-EDS) enabled the precise classification of individual floc constituents that cannot be achieved via SEM-EDS.

2.4. Acquisition of Image Data

2.4.1. 3D µCT

µCT scans were performed using a Nikon Metrology XT-H 225 (Tokyo, Japan) micro-tomograph. This scanner was configured with a 25-225 kV 0-2000 µA X-ray source with tungsten reflection target capable of generating polychromatic X-rays (focal spot size, c. 3 µm), and a Perkin Elmer (Waltham, Massachusetts, USA) 16-bit flat-panel detector. Scan parameters were set to optimise contrast and resolution (voltage 150 kV; current 160 µA; acquisition time between projections 2829 ms) with 2-frame averaging. Maintaining the same scan parameters for all µCT scans ensured comparability between datasets. The greyscale values of resulting

projections represented differences in X-ray energy attenuation, related to material density and the attenuation coefficient of the materials being imaged.

2.4.2. 2D SEM, STEM and EDS

2D SEM image montaging (block-face SEM) was conducted using an FIB-SEM (FEI Quanta 3D FEG, Hillsboro, Oregon, USA) fitted with a low-kV backscattered electron detector. Backscattered electron (BSE) images were collected at 3 kV accelerating voltage and 4 nA beam current to minimise the electron beam interaction volume and improve the spatial resolution of the BSE signal. Greyscale contrast of BSE images typically reflects composition. Systematic imaging of the floc cross-section generated 100's of images (pixel resolution, c. 30 – 60 nm^2). Images were subsequently stitched together into montages using the Grid/Collection Stitching plugin in open source software FIJI/ImageJ (Preibisch et al. 2009).

SEM-EDS elemental maps, STEM images and STEM-EDS point spectra were obtained using an FEI Inspect-F SEM fitted with a split field STEM detector (Hillsboro, Oregon, USA) and equipped with an Oxford Instruments (Oxford, UK) INCA X-act energy dispersive X-ray spectrometer. For low-resolution SEM-EDS mapping of the entire floc cross-section and high-resolution elemental mapping of RoI (see section 2.3) an accelerating voltage of 10 kV (counting period, 10 – 30 min). Counting periods varied between RoI and were selected to minimise damage to the sample surface. Dark-field STEM imaging of the ultrathin-sections was achieved at an accelerating voltage of 30 kV. Point spectra (STEM-EDS) were obtained from individual particles, at an accelerating voltage of 10 kV.

2.4.3. 3D FIB-nt Data Volumes

3D FIB-nt was performed using a FIB-SEM (FEI Quanta 3D FEG, Hillsboro, Oregon, USA) following the protocol outlined by Bushby et al. (2011). This relied on using the automated serial sectioning and imaging software Slice & View software (FEI Hillsboro, Oregon, USA). Experimentation revealed an accelerating voltage of 30 kV and a current of 0.5 – 5 nA for the ion beam to be optimal for milling. Images were captured using the BSE signal detector operated at a voltage of 3 kV and current of 4 nA, selected to match those used for 2D SEM (see section 2.4.2). The accuracy of FIB-nt relies on the stability of the FIB during milling and its ability to maintain regular intervals (i.e. slice thicknesses) between consecutive slices. An automated correction algorithm was applied during the serial sectioning procedure, which reduces or eliminates drift phenomena.

2.4.4. Reconstruction and Segmentation of the 3D Data

The product of µCT and FIB-nt are 2D projections/images of the sample/volume of interest that must be reconstructed to generate 3D volumes for visualisation and quantification. The reconstruction of µCT datasets was conducted using CTPro 3D (Nikon, Tokyo, Japan). Each scan generated 1,609 raw X-ray projections, yielding volumes with dimensions of 1,024 × 1,024 × 1,024 voxels (voxel size resolution, 10 μm^3). During reconstruction artefacts (e.g., beam hardening, Ketcham & Carlson 2001) were addressed by the application of specific algorithms. FIB-nt datasets were reconstructed following the protocol outlined by Bushby et al. (2011) using FIJI/ImageJ v2 (Schindelin et al. 2012). The number of images comprising FIB-nt datasets varied depending on the size of the analysed volume, ranging between 400

– 600 images. During setup for FIB-nt the mill thickness was adjusted to match the pixel resolution of the images, ensuring an isotropic voxel size suitable for quantitative analysis (Bushby et al. 2012).

2.4.5. Visualisation and Quantification of the Correlative Datasets

The quantification and visualisation of both µCT and FIB-nt datasets was conducted in in FIJI/ImageJ and required material segmentation, i.e. the classification of material phases based on greyscale values and/or shape, a critical stage in image processing (Cnudde & Boone 2013). Segmentation was achieved via greyscale thresholding or using a semi-automated segmentation tool plugin (Trainable WEKA Segmentation, TWS v2.1.0) capable of machine learning (Arganda-Carreras et al. 2017). The choice between these segmentation methods was guided by appraisal of dataset complexity, including the number of bulk phases and the overlap between phase greyscale envelopes common in natural environmental materials. Resulting binary volumes were then quantified using the 3DRoiManager plugin (Ollion et al. 2013), which provided quantitative measurements of material properties, e.g., size, shape and greyscale intensities etc.

2.4.6. Co-Registration of Datasets

The process of aligning multiscale datasets (i.e. co-registration) is a critical aspect of the correlative workflow, allowing information obtained using different imaging modalities and different spatial scales to be directly related. Co-registration of the multiscale 2D/3D datasets was achieved in the visualisation software Avizo (FEI Visualisation Sciences Group, Berlin, Germany). The success of registration is dependent upon the identification of fiducial markers in the different datasets. Co-

registration of µCT datasets relied upon the identification of the aluminium wire implanted within the resin block, whilst internal landmarks (e.g., silt particles, bacteria etc.) were used in the co-registration of higher resolution 2D and 3D datasets. Fig. 1 shows the sequence of steps taken to co-register the correlative datasets. Coarse alignment was manually conducted using the Transform Editor tool within Avizo, while fine registration was conducted automatically using the Landmark Surface Warp module applied using a rigid transformation algorithm.

3. Results and Discussion

3.1. Overview of the Multiscale Datasets

3.1.1. 3D Floc Sub-mm Structure and Internal Density

Volumetric renderings of three floc samples (FS1, FS2 and FS3) generated based on the µCT data (resolution, c. 10 μm^3) are shown in Fig. 2. For each 3D reconstruction greyscale contrast (16-bit pixel depth, e.g., 65,536 greyscales) between the flocs, surrounding resin and aluminium fiducial markers was sufficient to allow segmentation based on simple thresholding. This is illustrated in Fig. 1a and b that show cross-sectional greyscale images taken from the reconstructed µCT scan of FS1, in which the floc and surrounding resin are easily distinguishable. Scan parameters were kept constant for each of the flocs, and thus datasets are directly comparable. Table 1 details the criteria (e.g., greyscale range, size and shape etc.) for identify the different material phases; i) resin ii) floc, and iii) aluminium registration pin. The result of the segmentation procedure was a binary masks which formed the basis for subsequent visualisations and quantitative analysis (Fig. 2 and Table 2).

Quantitative analysis of the floc samples showed FS2 to have the largest volume, with a total occupied volume (i.e. voxel count) of 5.04×10^8 µm (Table 2).

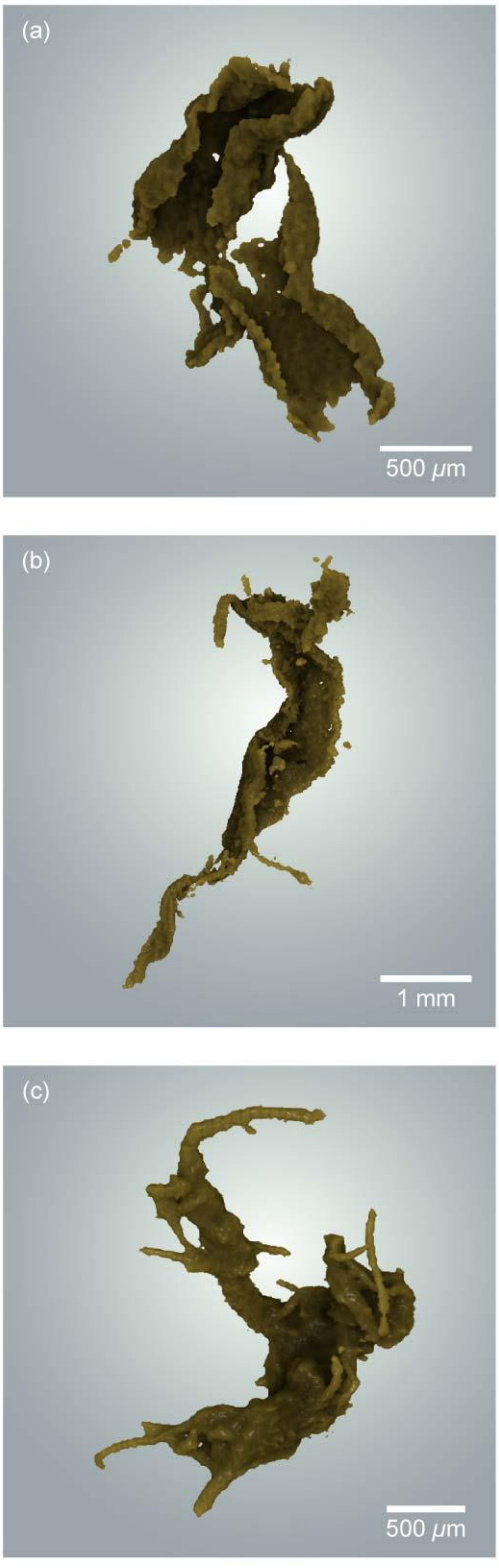

Figure 2. 3D visualisations of the floc samples FS1 (a) and FS2 (b) and FS3 (c) generated in Drishti from X-ray µCT data.

334 Descriptions of floc diameter (*D*) and height to width ratios (H/W) were made using
335 the Feret diameter, i.e. the distance between two parallel planes enclosing an object.

Based on these the floc samples can be described as macroflocs (*D*>160 µm; Manning & Dyer 2002) that exhibit elongate (H/W >2:1) and highly contorted morphologies. Flocs FS2 and FS3 exhibit filamentous protuberances projecting beyond their peripheries, likely related to the presence of cyanobacteria (confirmed by SEM, STEM and FIB-nt dataset, see sections 3.1.2, 3.1.3 and 3.1.4). FS1 was observed to differs significantly from FS2 and FS3, being composed of three distinct sub-units, connected by narrow linkages c. ≤30 µm. Each of the floc samples exhibited regions of high and low X- ray attenuation (Table 1 and Fig. 2c and Fig. S2 of Supplementary Materials). The distribution of regions of high attenuating elements within floc FS2 are shown in a 3D rendering in Fig. S2 of Supplementary Materials. This information provided a means of identifying RoI for further analysis (see Section 3.1.2 and Fig. 3a-c and Fig. S3 of Supplementary Materials).

Floc Sample	Floc Volume (μm^3)	Feret Diameter (µm)			H/W
		Major	Intermediate	Minor	
FS1	1.95×10^8	2414.54	1298.65	631.29	3:1
FS2	5.04×10^8	11183.83	755.82	266.06	4:1
FS3	2.44×10^8	945.03	800.19	323.23	2:1

Table 2. 3D quantitative measures of floc geometry (volume and Feret diameter) and shape (height/width ratio).

3.1.2. 2D Floc Micrometre-Structure and Composition Revealed in Cross-Section

Fig. 3c shows the 2D SEM-BSE image montage collected from the cross-section of floc FS1 (resolution, c. 60 nm^2), (FS2, resolution, c. 30 nm^2 and individual SEM-EDS

elemental maps are shown in Fig. S2 and Fig. S4 respectively). Similar to µCT, greyscale contrast (8-bit pixel depth, e.g., 256 greyscales) was sufficient to allow flocculated material to be segmented from surrounding resin. However, the higher resolution of SEM also enabled the recognition of additional floc components, which could be classified based on particle size, shape and greyscale value and further validated by comparison with SEM-EDS elemental maps. Four additional materials were identified; i) resin filled pore-space, ii) floc matrix (e.g., clays, unicellular bacteria, organo-mineral debris), iii) individual non-clay mineral grains (e.g., quartz, feldspar and mica) and iv) large bio-organic and organic structures (e.g., organic detritus, diatoms, cyanobacteria) (Table 1 and Fig. 3d). Particles <10 µm (e.g., EPS,

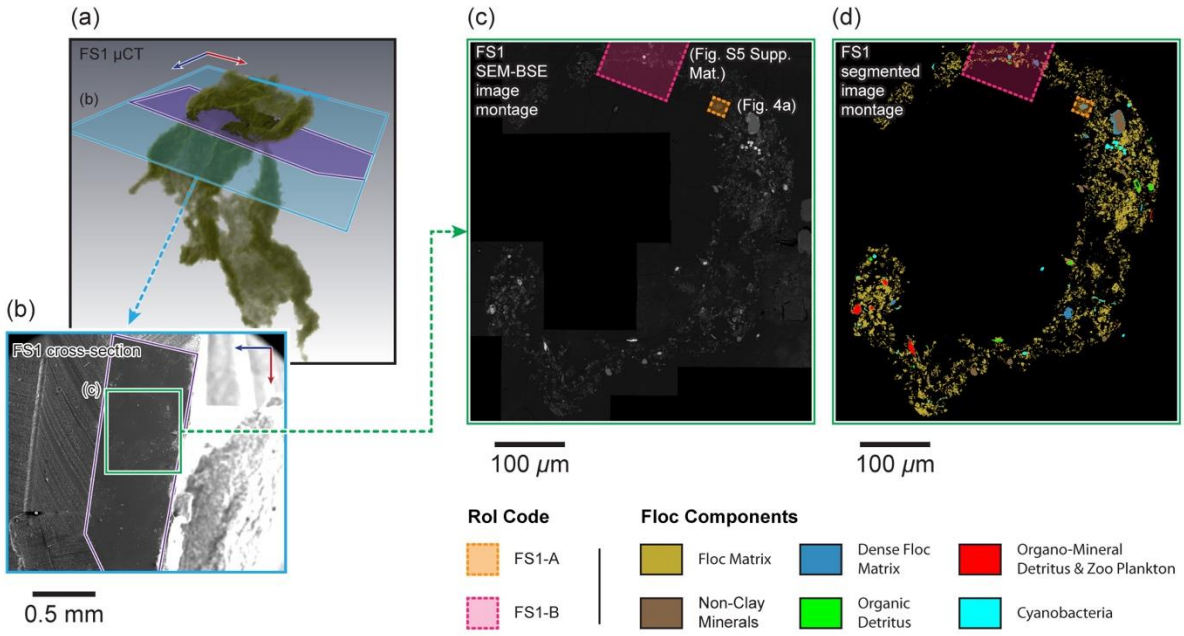

Figure 3. Analysis of the cross-section located in floc FS1. The location of the cross-section created within FS1 is shown in (a) and the region of the cross-section containing the floc is shown in (b). The trapezoidal shape of the sectioned block is highlighted in purple both in (a) and (b), while the boundary of the SEM image of the cross-section shown in (b) is defined in 3D space in (a) in blue. The SEM-BSE image montage (c) obtained from the cross-section through floc FS1 enabled the identification of floc constituents (d) and characterisation of floc structure in 2D. The locations of RoI selected for further analysis are shown in (c) and (d).

366 clay minerals and unicellular bacteria) could not be accurately segmented and were
367 identified collectively as ‘floc matrix’. The floc matrix is likely to be compositionally
368 complex, however, SEM-EDS revealed strong signals for Fe, Al/Si and Si (Fig. S4 of
369 Supplementary Materials), indicating the presence of iron oxyhydroxides, clay
370 minerals and silicates. Constituents were unevenly distributed within the floc matrix,
371 with regions of low occupation characterised by high porosity and low greyscale
372 values (c. <50) and regions of high occupation exhibiting low porosity and high
373 greyscale values (c. >70) (Fig. 3 and Table 1).

374 Non-clay mineral grains were differentiated based on their blocky/irregular
375 morphology, uniform greyscale and elemental signature (Si, Fe). In comparison, bio-
376 organic material and biota could be identified relatively easily based on their high
377 greyscale values (c. 200 – 255) due to heavy metal (Pb, Os and U) staining (see
378 also elemental phase map, Fig. S4 of Supplementary Materials). Strong signals for
379 Pb, Os and U related to heavy metal-stained organics, typically large features
380 (diameter, >10 µm) such as cyanobacteria and organic detritus, while an associated
381 signal of Si (blue) was indicative of eukaryotic plankton (e.g., diatom, foraminifera).

382

383 **3.1.3. 2D Submicrometre and Nanometre Structure and Composition of**
384 **Selected RoI**

385 For each floc several RoI were identified based on structural and/or compositional
386 characteristics revealed in SEM-BSE imagery and SEM-EDS elemental maps (see
387 Section 3.1.2). Fig. 3 and Fig. S3 of Supplementary Materials show the locations of
388 RoIs selected for FS1 and FS2 respectively. RoIs were targeted to either
389 characterise further floc nm composition and particle-particle interactions via STEM,

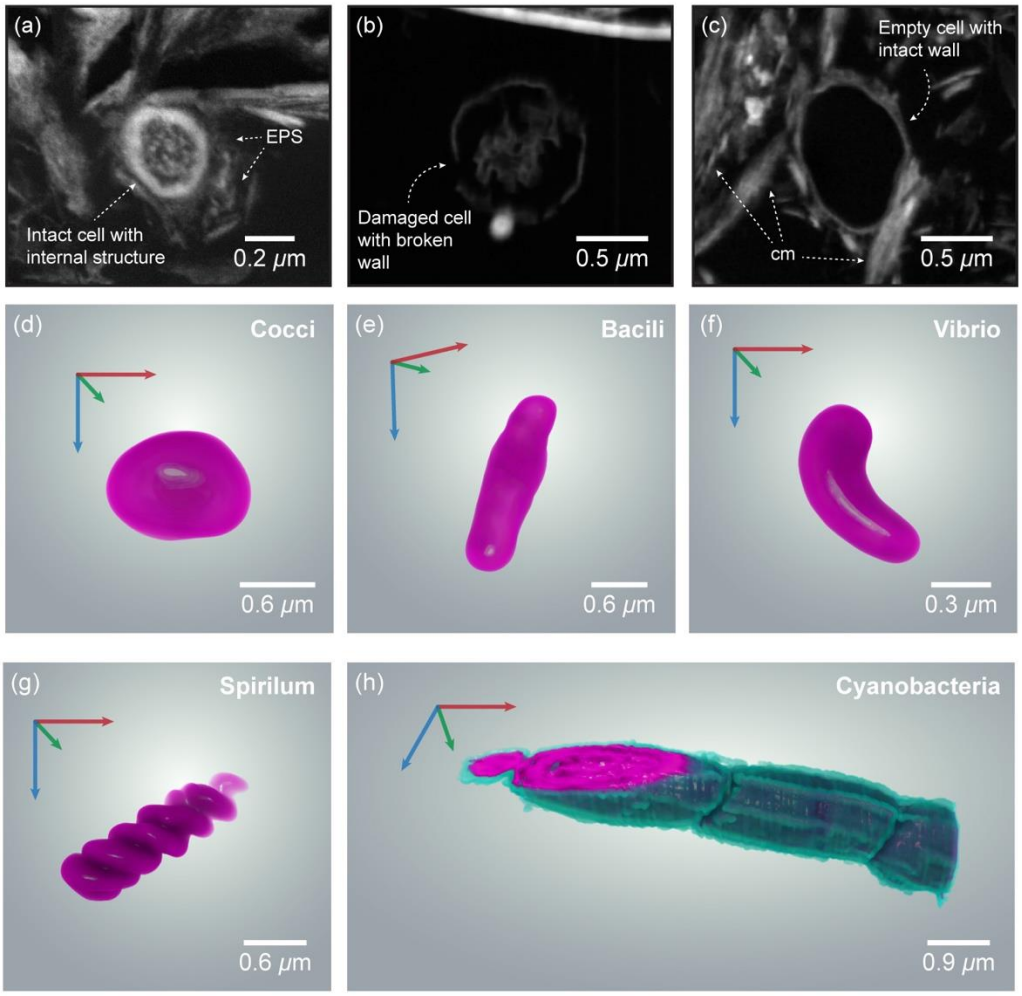

Figure 5. Characterisation of bacterial cells. (a – c) STEM images showing examples of the three categories of intracellular integrity used as an indicator of the fidelity of stabilised flocs to their original structure. (d – g) Examples of different bacterial cellular morphologies reconstructed based on 3D FIB-nt data. (a) intact bacteria displaying an undamaged cell wall, cytoplasm (grainy structure) and nucleoplasm (denser region towards the centre of the cell); (b) damaged bacterial cell with a broken cell wall and degraded cytoplasm and/or nucleoplasm; (c) empty cell lacking plasma. (d) cocci, (e) bacilli, (f) vibrio, (g) spirillum and (h) cyanobacteria.

or selected for SEM imaging to define submicrometre structure. Selected SEM-BSE (resolution, c. 25 - 30 nm^2) and STEM (resolution, c. 5 - 10 μm^2) imagery and corresponding SEM-EDS elemental maps are shown in Fig. 4 and Fig. S5 of Supplementary Materials.

394 The four main floc constituents (pore-space, floc matrix, non-clay mineral
395 grains, and large bioorganic and organic structures) were also identified in SEM-BSE
396 and STEM imagery. However, the higher resolution enabled further distinction
397 between materials within the floc matrix: i) clay minerals, ii) microbial cells, iii)
398 organo-mineral debris, and iv) EPS (Table 1). Microbial cells could be easily
399 identified due to their high greyscale values (c. >200) and differential staining of
400 subcellular structures (Fig. S5 of Supplementary Materials). High-resolution STEM
401 imagery revealed internal/external cell structure allowing the classification of
402 microbes based on their metabolic state (Heissenberger et al. 1996) as: i) intact, ii)
403 damaged and iii) empty (e.g., Fig. 5a – c). Whilst the resolution of SEM imagery
404 prevented the detection of EPS 2 – 20 nm in diameter (Leppard 1992), its presence
405 is confirmed by STEM imagery (Fig. S6 of Supplementary Materials). EPS was
406 observed to be closely associated or 'bound' to the cell walls of metabolically active
407 microbes, whilst 'soluble' EPS exuded by microorganisms was found throughout the
408 floc matrix and often associated with clay minerals (Fig. S6 of Supplementary
409 Materials).

410 To investigate density variations within the floc matrix (see Section 3.1.2, Fig.
411 3 and Figs. S3 and S4 of Supplementary Materials), RoIs FS1-A and FS2-B (Fig. 4a
412 and e) were selected to encompass regions exhibiting high and low occupation.
413 Within both high and low occupation regions clay minerals were rarely observed in
414 isolation, but were observed in units of 10's of particles. STEM imagery revealed
415 several common particle associations, including units of clay platelets aligned face-
416 to-face and/or edge to face, and clay minerals arranged around a central bacterium
417 (Fig. S6 of Supplementary Materials). Low density regions of the floc matrix mainly
418 consisted of particle associations arranged in open, 'card-house' structures, and

were highly porous (Fig. 4a). STEM showed the nanometre pore space between primary particles filled with exopolymeric material, whilst EPS was notably absent in the larger micrometre pore channels (Fig. S6 of Supplementary Materials). In comparison, high density areas consisted primarily of closely packed clay minerals dispersed with pyrite (Fe+S) (Fig. 4c), and had a lower porosity and high organic signal (Fig. 4d).

3.1.4. 3D Submicrometre-Structure and Composition of Selected RoI

Volumetric renderings of two FIB-nt volumes obtained from FS2, labelled FS2-A and FS2-B and corresponding to the RoI of the same name (see Fig. 4e and Fig. S5 of Supplementary Materials), are shown in Figs. 6 and 7 respectively. The large volume size of FS2-A (c. 8×10^4 μm^3, voxel size c. 67 nm) enabled the organisation of large submicrometre structures to be revealed in 3D, while the higher resolution of FS2-B (c. 5×10^3 μm^3, voxel size c. 15 nm) allowed for the detailed characterisation of constituents and particle-particle associations.

FIB-nt datasets were segmented following Wheatland et al. (2017). The primary floc constituents (resin filled pore-space, floc matrix, non-clay minerals, and large bioorganic and organic structures) and floc matrix constituents (clays minerals, microbial cells and organo-mineral debris) identified in 2D SEM and STEM were also identified in FIB-nt (Table 1 and Fig. 6 and 7). Additionally, the enhanced spatial resolution of FS2-B enabled the segmentation of closely packed particles c. <2 µm (e.g., clays within the floc matrix), enabling their reconstruction in 3D (Fig. 7e). This is demonstrated in Fig. 7d in which individual clays can be discriminated in 2D slices from the FIB-nt dataset. Several of the particle-particle associations identified within SEM and STEM data (see Section 3.1.3 and Fig. S6 of Supplementary Materials)

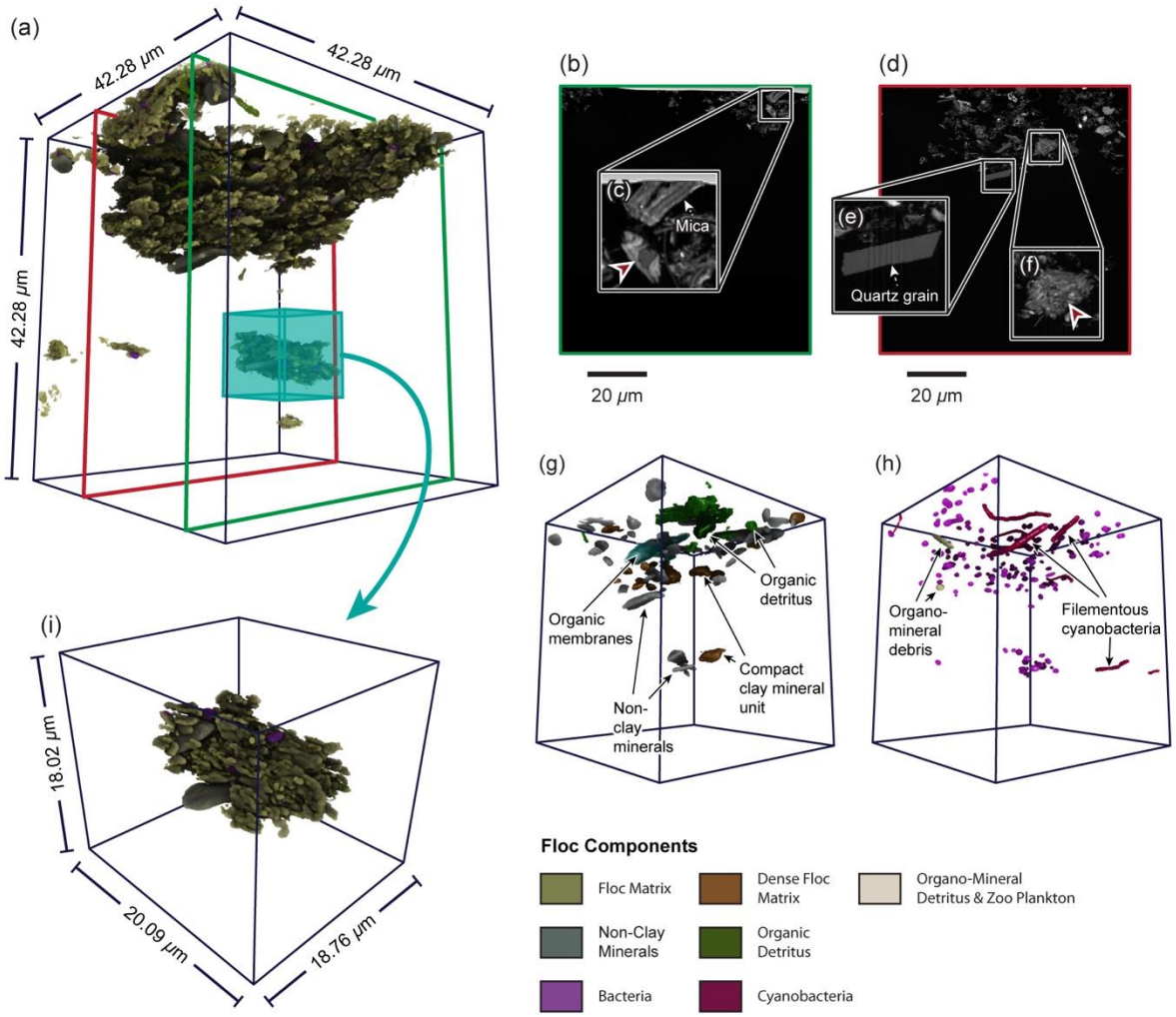

Figure 6. 3D reconstructions of the FIB-nt volume RoI FS2-A: (a) 3D rendering of the segmented components identified within FS2-A; (b - c) Selected BSE images from the FIB-nt dataset illustrating the differences in grey-scale and morphology that enable feature segmentation, note the red arrow shown in (c) highlights a region of high particle occupation. The locations from which the 2D BSE images shown in (b) and (c) were taken from within the FIB-nt dataset are indicated by coloured lines shown in (a); (g) Same as (a) but with selected materials rendered transparent to reveal the non-clay minerals, organic membranes and amorphous organic detritus; (h) Same as (a) but with certain materials rendered transparent to reveal the individual bacteria, cyanobacteria and organomineral debris (diatom frustules); e)) Sub-volume taken for FS2-A showing an isolated microfloc (location indicated in (a)).

were also identified in FS2-B. Visualised in 3D these structures are revealed to be discrete units, separable from surrounding floc matrix by nanopores (Fig. 7e and f).

Fig. 7e shows a particle association consisting of clay minerals aligned face-to-face, while Fig. 7f shows clay particles aligned around a central bacterium. Examination of the floc matrix reveals micrometre pore channels delineating the boundaries of discrete structural units 10's μm in diameter (e.g., Fig. 6i). These structures usually consist of several particle-particle associations and larger primary particles (e.g., silt grains, organic detritus), loosely arranged in an open, card-house structure, linked together by filamentous cyanobacteria.

Quantification reveals the occupied volume of FS2-A largely consists of inorganic material, with clays accounting for c. 98% of occupied space and non-clay minerals c. 0.5% (Table 3). In contrast, a larger proportion of FS2-B is occupied by organics, which accounted for c. 34% of the occupied volume compared to inorganic material, c. 66%. Within both FIB-nt datasets micrometre pore channels can be identified together with elongated nanopores throughout the floc matrix (Fig. 6 and 7). Combined, these give a total porosity of c. 95 % and c. 52 % for FS2-A and FS2-B respectively. The resolution and 3D nature of the datasets enabled the classification of microbial cells based on morphotype (Dazzo & Niccum 2015) and five categories were recognised: i) cocci, ii) regular straight rods (e.g., bacilli), iii) curved/U-rods (e.g., vibrio), iv) spirals (e.g., spirilla) and v) unbranched filaments (e.g., cyanobacteria) (Fig. 6d - h). Cocci were characterised as near spherical (length/width, <2:1) with diameters <1.5 μm (Fig. 6h), frequently forming groups of several cells. In comparison, bacilli exhibited a straight, rod-like morphology (length/width, <16:1) and were larger (diameter, c. 2 μm). Cells with a crescent curvature (comma-shaped) were identified as vibrio, and had similar dimensions to bacilli (Fig. 5d – h). Although observed less frequently, spirilla were classified as elongated cells displaying a distinctive repeated waveform (e.g., corkscrew-shaped).

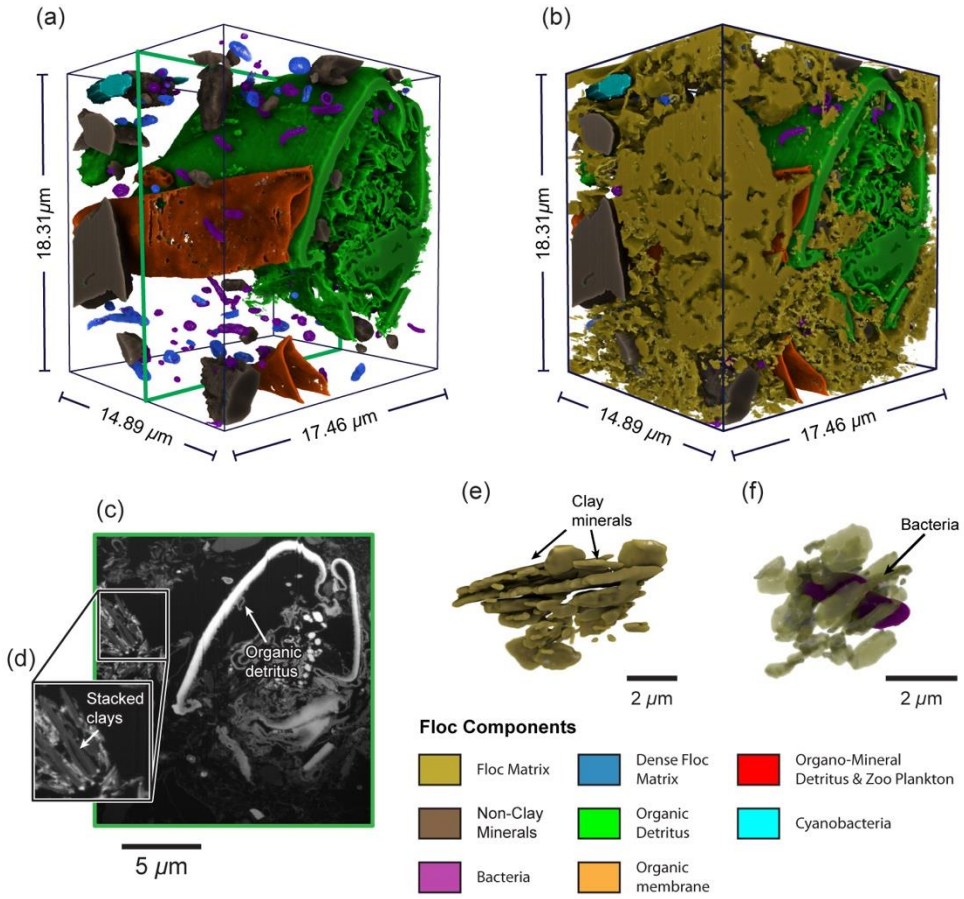

Figure 7. 3D reconstructions of the FIB-nt volume RoI FS2-B: (a) 3D rendering of the segmented components identified within FS2-B; (c) Selected BSE image from the FIB-nt dataset illustrating the differences in grey-scale and morphology that enable feature segmentation. The locations from which the 2D BSE image shown in (c) was taken from within the FIB-nt dataset are indicated by the green coloured line shown in (a); (d) Sub-set from (c) showing clay minerals aligned face-to-face and/or edge-to-face; (e) 3D reconstruction of (d); (f) Clay particle arranged radially around a bacterial cell (bacteria false-coloured purple).

Filamentous (cyanobacteria) bacteria could be easily distinguished from other cell types based on elongated shape (length/width, >16:1), and were present in a number of forms, ranging from cells 1 – 2 µm in diameter to larger varieties (diameters, c. >3 µm) (Fig. 5h). The quantities of cell morphotypes and their intracellular integrity (e.g., intact, damaged or empty, Heissenberger et al. 1996) are shown in Table 4.

FIB-nt Sample	Total Volume (μm^3)	Floc Constituents (Vol. %)						
		Porosity		Floc Matrix			Other	
		Micro-Porosity	Nano-Porosity	Clay Minerals	Bacteria	Organo-Mineral Debris	Organic Detritus	Non-Clay Minerals
FS2-A	c. 8×10^4	91.4	3.80	4.08	0.07	0.01	0.23	0.41
FS2-B	c. 5×10^3	-	51.79	31.96	0.45	0.07	17.16	2.15

Table 3. Volume fractions for the segmented components of FIB-nt datasets FS2-A and FS2-B.

FIB-nt Sample	Total Bacteria (Count)	Intracellular Integrity (% of Total Count)		Cell Morphotype (% of Total Count)				
		Intact Cells	Damaged and Empty Cells	Cocci	Regular Straight Rod	Curved/U-Rod	Unbranched Filament	Spiral
FS2-A	239	73.2	26.8	48.95	28.03	17.57	5.44	0
FS2-B	118	76.4	23.6	41.53	32.20	19.49	4.24	2.54

Table 4. Total count of bacteria, numbers of intact, damaged and empty cells and proportions of different cell morphotypes identified in FIB-nt datasets FS2-A and FS2-B.

3.2. Validation of Floc Stabilisation Method

Interpretation and quantification of 3D flocs relies on an assumption that the characteristics observed are representative of true floc structure and not artefacts of sampling, storage and preparation (Liss et al. 1996; Wheatland et al. 2017). The correlative workflow demonstrated above permits the validation of floc integrity in this context by enabling observation of 3D floc structure across multiple spatial scales.

Fluid exchanges and sample dehydration are essential for the chemical stabilisation process, but can result in the distortion and/or rupture of delicate cellular structures. While a number of cells identified in the 3D FIB-nt datasets were classified as either damaged or empty (Heissenberger et al. 1996) (Table 4), Wheatland et al. (2017) notes that the presence of damaged cells in itself is not indicative of inadequate stabilisation, since active microbial communities contain cells of all states of life including decay. More diagnostic of the state of preservation is the presence of intact cells, as rupture due to poor stabilisation would be expected to be systemic. Within the FIB-nt datasets intact cells accounted for c. >50% of the total number of cells, a higher percentage compared than that of the total number of metabolically active bacteria usually found in natural microbial communities (c. <30%, Ward & Johnson 1996). The loss of soluble EPS (i.e. EPS unassociated with bacterial cells) from the floc matrix during fluid exchanges can result in severe perturbation (Leppard et al. 1996). Previous studies have estimated up to 50−80% of EPS can be removed in certain instances from the floc matrix following stabilisation (Leppard et al. 1996), with the primary effect on the floc being the rearrangement of primary particles and compression of floc structures (recorded as shrinkage) (Liss et al. 1996). STEM imagery obtained from the floc samples reveals the presence of exopolymeric material, observed as dense networks in the nanometre pore space between primary particles (e.g., clays and bacteria) and distributed throughout the floc matrix (Fig. S6 of Supplementary Materials). This suggest that the little extraction of the EPS network within the floc matrix has taken place. The use of plankton chambers for floc capture and agarose gel for floc immobilisation help minimise the destructive forces associated with traditional sampling methods (e.g., floc breakage via pipetting) (Droppo et al. 1996). However, morphological changes

516 can result if flocs interact once settled, e.g., false aggregation of flocs and/or
517 pseudoplastic contortion of delicate structures with overburden pressure.
518 Examination of flocs of immobilised in agarose prior to resin embedding provides a
519 means of assessing the degree of interaction between neighbouring flocs. 2D cross-
520 sectional images taken from the µCT of test sample FS0 (Fig. S1 of Supplementary
521 Materials) reveal minimal overlap between neighbouring floc particles, suggesting
522 morphological changes to be minimal. This is supported by the 3D visualisation of
523 individual flocs (FS1, FS2 and FS3, Fig. 3 and Movie 1) that indicate delicate
524 structures (e.g., filamentous protuberances, Fig. 3b and c) remained intact following
525 settling and during the addition of agarose and sub-sampling for stabilisation.
526

527 **3.3. Merits of the Correlative Workflow**

528 This imaging workflow enables for the first time floc composition and 3D structure to
529 be investigated at all relevant spatial scales, from primary particles to entire flocs
530 several mm in size. This represents a significant advance in our ability to
531 characterise flocs, filling the resolution gap between traditional imaging techniques
532 (e.g., TEM, CLSM and COM) (Fig. 8).

533 The success of the workflow critically depends upon the quality (i.e. resolution,
534 signal-to-noise ratio) and degree of similarity (i.e. resolution and mechanisms for
535 contrast generation) between the different datasets (Caplan et al. 2011; Handschuh
536 et al. 2013). Image quality is of particular importance, since it determines the
537 accuracy with which features can be identified, segmented and quantified. Within
538 µCT and EM datasets the boundaries between objects are not always well defined,
539 but can consist of a transitional zone 3 – 5 pixels wide (Holzer et al. 2014;
540 Wheatland et a. 2017). Depending on the pixel/voxel resolution of the dataset the

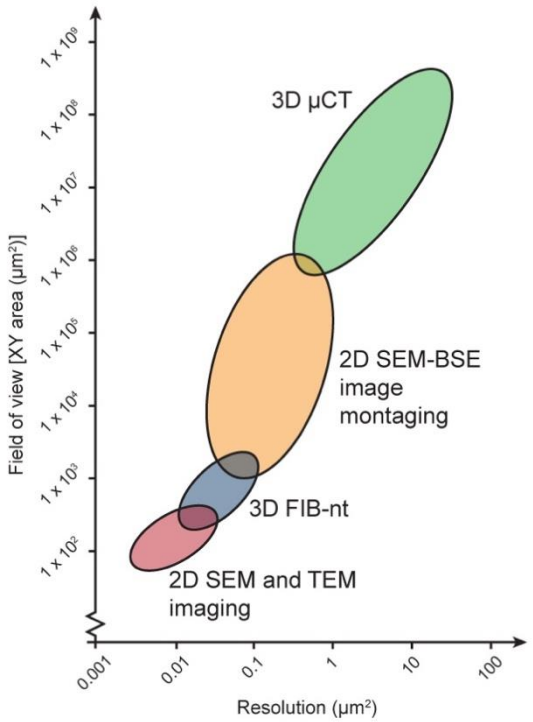

Figure 8. Length-scales over which the 2D and 3D imaging techniques employed within correlative workflow operate, with corresponding typical cross-section (XY) and resolution achievable by each technique. Note that the imaging methods used overlap, enabling truly correlative examination of floc structure from the nm to mm-scale.

maximum error is usually considered to be half the width of this zone. Further discussion regarding the process of segmentation and potential errors is outlined in Wheatland et al. (2017).

Fig. 3 shows the correlative 2D and 3D datasets collected from FS1 registered in a single 3D scene. To locate the floc cross-section, aluminium wire was used as a fiducial marker to register the µCT data collected after ultramicrotomy to the original µCT dataset of the intact flocs (see Section 2.3 and Fig. 1d). Segmentation of the

548 aluminium wire would ideally result in it being represented by similar number voxels

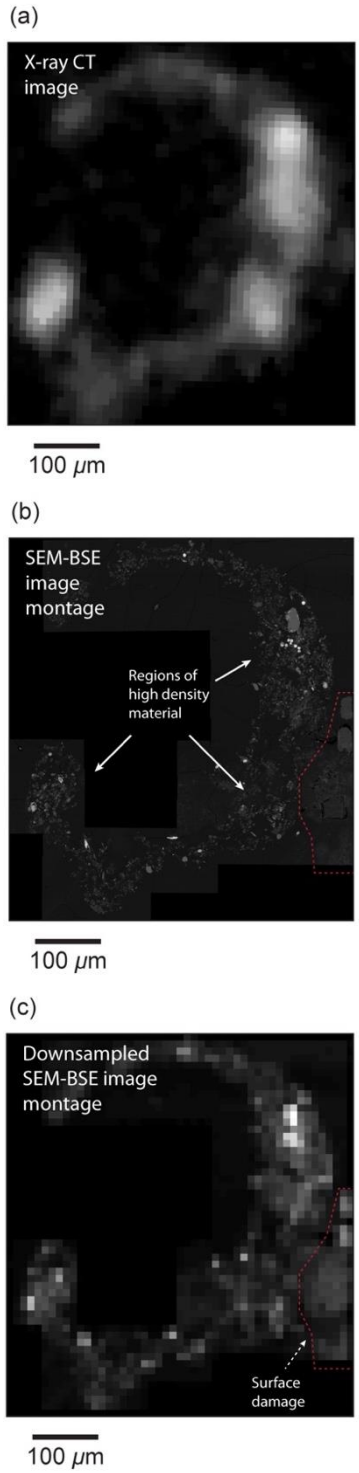

Figure 9. Comparison of µCT with SEM-BSE. Down-sampling the pixel size of the SEM-BSE image montage (c) to match that of the µCT data (c. 10 µm), enabled comparison between the SEM-BSE image montage (b) and corresponding µCT slice (a). This provides a means of validating the potential floc structures responsible for different greyscale values within the µCT dataset. Regions of the floc observed to contain high concentrations highlighted in (b) of particles in the BSE-SEM image montages were shown to exhibit high grey-scale values in the µCT dataset (a).

549 in the corresponding µCT datasets. Within both pairs of µCT data the wire was easily
550 segmented from other material phases based on its high greyscales (e.g., see
551 Section 3.1.1 and Fig. 2). However, discrepancies in the size of the segmented
552 aluminium wire were observed – 1.6% for FS1 and 3.8% for FS2 – which likely
553 resulted from scan artefacts, i.e. secondary edge effects due to partial volume effect.
554 Assuming an even distribution of the extraneous voxels around the surface area of
555 the aluminium fiducial marker, the minimum offset between co-registered datasets
556 can be estimated to be of the order of less than a voxel (c. 3 – 6 µm) over a total 3D
557 size of 10×10^8 µm. With evidence of only minor peripheral misalignment of the
558 registered datasets, the co-registration of the 3D µCT scans has been successful.
559 2D SEM-BSE image montages of the floc cross-sections were critical for the
560 co-registration of 2D and 3D nm and µm datasets with the sub mm-scale 3D µCT
561 data. The trapezoidal shape of the cross-sections (Fig. 3b and Fig. S3 of
562 Supplementary Materials) can be defined in the µCT datasets, enabling the SEM-
563 BSE image montages to be tied to the surface within an accuracy of 3 – 6 voxels (c.
564 30 – 60 µm). However, further confidence in the accuracy of the co-registration can
565 be obtained by comparing the actual shape of the floc boundary depicted in the two
566 datasets. Reducing the pixel resolution of the SEM-BSE image montages (i.e. down-
567 sampling) to match that of the µCT datasets (c. 10 µm) enables a direct comparison
568 between the SEM-BSE image montages and µCT data (Fig. 9), which indicates the
569 error to be less than a voxel (c. <10 µm). In addition, the features responsible for the
570 variations observed in µCT greyscale values, that reflect the variability of floc
571 constituents and structure at the sub-voxel scale (representing the impact of partial
572 volume effects, cf. Ketcham & Carlson 2001), can be confirmed by comparing the
573 down-sampled SEM-BSE image montage with the corresponding µCT slice. Fig. 9

demonstrates that regions of the SEM-BSE image montage identified as containing high concentrations of particles correspond to regions of high attenuation (high greyscales) within µCT. The similar imaging conditions selected for both SEM-BSE imaging (montaging and imaging of RoI) and FIB-nt allowed reference landmarks within the corresponding datasets to be recognised with a high degree of certainty (20 – 60 nm). As the contrast mechanisms in both SEM-BSE and dark-field STEM are similar (related to atomic number) fiducial markers internal to the floc (e.g., silt grains and bacteria etc.) could be easily identified. However, inspection of the overlaid STEM images following co-registration with SEM imagery revealed discrepancies in the positions of these markers. These displacements are likely the result of ultramicrotomy, as shear stresses imposed during sectioning are known to cause thin-section compression (Peachey 1958).

3.4 Applications of 3D Floc Structural and Compositional Data

Providing such detailed 3D analysis of flocs is not readily applicable for field scale quantification of suspended sediment aggregates. However, this technique has the potential, through targeted experimental or field campaigns, to provide new understanding of floc composition and controls on floc characteristics and structures. For example, these datasets quantify 3D floc characteristics (e.g., size, shape and porosity) that are critical input parameters to cohesive sediment transport models.

Additionally, the datasets demonstrate the complex structural associations and particle-particle interactions found at different spatial scales and levels of aggregation. These are frequently hypothesised in the literature or inferred from 2D observations of gross floc characteristics (e.g., Maggi et al. 2007; Lee et al. 2011). These particle-particle associations reflect the materials present in suspension

599 during floc development and their interactions. Here, the particle associations
600 including clays oriented face-to-face and/or edge-to-face likely occur due to a
601 combination of electrochemical interactions (i.e. cohesion), and the additional
602 binding forces provided by organic materials resulting in bioflocculation, i.e. adhesion
603 (Liss et al. 1996; Righetti & Lucarelli 2010). Yet the short distances (10^1 to 10^3 nm)
604 over which these forces (cohesion and adhesion) operate mean that these structures
605 are clearly scale-dependent. Larger structural units consisting of several particle-
606 particle associations and individual primary particles (e.g., silt grains, amorphous
607 organic detritus etc.) were found throughout the floc samples. Therefore, this new
608 method could provide data to challenge or validate simplified descriptors of floc
609 structure e.g., self-similarity or fractal geometry (e.g., Khelifa & Hill 2006).
610 Our data also demonstrate and quantify the microbial associations with
611 flocculated material. For example, demonstrating the importance of cell morphotype
612 on floc shape and strength. Here, filamentous cyanobacteria cross-link smaller
613 structural units (observed in 2D SEM and 3D FIB-nt) promoting interactions between
614 these structural units and providing structural connectivity and flexibility (e.g.,
615 Nguyen et al. 2007). Their strongly elongate shape and propensity to align has a
616 strong influence on floc development, promoting the growth of non-spherical flocs.
617 Additionally, filaments extending from the periphery of the flocs provide anchor
618 points to facilitate floc growth through interactions with other flocs (Burger et al
619 2017).
620
621 **4. Conclusion**
622 The development of a novel correlative workflow provides datasets demonstrating
623 the complex composition and multiscale 3D structure of aquatic sediment flocs. This

work provides the most detailed floc structural analysis to date and provides the following specific advantages:

- 2D and 3D imaging techniques can be applied in a systematic manner to successfully obtain a complete set of overlapping, co-registered datasets from a single floc sample. The resultant datasets enable the identification and quantification of floc composition and structures across multiple length-scales. This approach improves on traditional 2D correlative microscopy by providing truly correlative datasets that are quantifiable.
- The orientation of multi-scale and multi-modal datasets in 3D space presents a significant challenge, but can be successfully overcome using fiducial markers. This is reliant on selecting imaging techniques that share similar contrast mechanisms, to ensure that landmark features can be detected at different spatial scales.
- Particle-particle and structural associations can be directly related across length-scales. Structures that are scale-dependent can be recognised, providing further evidence for interactions that have previously been hypothesised. The imaging workflow therefore provides a means of obtaining quantitative measures of floc composition and structure and a better understanding of the mechanisms promoting floc growth.
- The correlative workflow is adaptable, and the potential exists for further research to design targeted experiments to explore relationships between floc structure and behaviour, controls on floc stability and structure, and floc microbial communities.

Acknowledgements

J.A.T.W. would like to thank the Engineering and Physical Sciences Research Council for the award of a scholarship and the Queen Mary University of London Postgraduate Research Fund. K.L.S, A.J.B and S.J.C acknowledge the Natural Environmental Research Council (NE/N011678/1) for funding. Jemima Burden (MRC Laboratory for Molecular Cell Biology, University College London) is thanked for her help with sample preparation.

References

Agrawal, Y.C., Pottsmith, H.C. 2000. Instruments for particle size and settling velocity observations in sediment transport. Mar. Geol. 168 (1–4), 89-114.

Arganda-Carreras, I., Kaynig, V., Rueden, C., Eliceiri, K.W., Schindelin, J., Cardona, A., Seung, H.S. 2017. Trainable Weka Segmentation: a machine learning tool for microscopy pixel classification. Bioinformatics 33 (15), 2424-2426.

Azam, F., Long, R.A. 2001. Sea snow microcosms. Nature 414, 495-498.

Burd, A.B. Jackson, G.A. 2009. Particle aggregation. Annu. Rev. Mar. Sci. 1, 65-90.

Burger, W., Krysiak-Baltyn, K., Scales, P.J., Martin, G.J.O., Stickland, A.D., Gras, S.L. 2017. The influence of protruding filamentous bacteria on floc stability and solid-liquid separation in the activated sludge process. Water Res. 123, 578-585.

Burnett, T.L., McDonald, S.A., Gholinia, A., Geurts, R., Janus, M., Slater, T., Haigh, S.J., Ornek, C., Almuaili, F., Engelberg, D.L., Thompson, G.E., Withers, P.J. 2014. Correlative tomography. Sci. Rep. 4, 1-6.

672 Bushby, A.J., Png, K.M.Y., Young, R.D., Pinali, C., Knupp C., Quantock A.J. 2011.
673 imaging three-dimensional tissue architectures by focused ion beam scanning
674 electron microscopy. Nat. Protoc. 6 (6), 845-858.
675 Bushby, A.J., Mariggi, G., Armer, H.E.J., Collinson, L.M. 2012. Correlative Light and
676 Volume EM: Using Focused Ion Beam Scanning Electron Microscopy to image
677 transient events in model organisms. Methods Cell Biol. 111, 357-382.
678 Caplan, J., Niethammer, M., Taylor, R.M., Czymmek, K.J. 2011. The power of
679 correlative microscopy: multi-modal, multi-scale, multi-dimensional. Curr. Opin.
680 Struct. Biol. 21 (5), 686-693.
681 Cnudde, V., Boone, M.N. 2013. High-resolution X-ray computed tomography in
682 geosciences: A review of the current technology and applications. Earth-Sci.
683 Rev. 23, 1-17.
684 Dazzo F.B., Niccum, B.C. 2015. Use of CMEIAS image analysis software to
685 accurately compute attributes of cell size, morphology, spatial aggregation and
686 color segmentation that signify in situ ecophysiological adaptations in microbial
687 biofilm communities. Computation 3, 72-98.
688 Droppo, I.G. 2001. Rethinking what constitutes suspended sediments. Hydrol.
689 Process. 15 (9), 1551-1564.
690 Droppo, I.G. 2003. A new definition of suspended sediment: implications for the
691 measurement and prediction of sediment transport. In: Bogen, J., Fergus, T.,
692 Walling, D. (Eds.), Erosion and Sediment Transport Measurement in Rivers:
693 Technological and Methodological Advances. IAHS Publication No. 249,
694 International Association of Hydrological Sciences, Wallinford, pp. 238.

695 Droppo, I.G., Flannigan, D.T., Leppard, G.G., Jaskot, C., Liss, S.N. 1996. Floc
696 stabilization for multiple microscopic techniques. Appl. Environ. Microbiol. 62,
697 3508-3515.
698 Handschuh, S., Baeumler, N., Schwaha, T., Ruthensteiner, B. 2013. A correlative
699 approach for combining microCT, light and transmission electron microscopy in
700 a single 3D scenario. Front. Zool. 10, 1-16.
701 Heissenberger A., Leppard, G.G., Herndl, G.J. 1996. Relationship between the
702 intracellular integrity and the morphology of the capsular envelope in attached
703 and free-living marine bacteria. Appl. Environ. Microbiol. 62 (12), 4521-4528.
704 Holzer, L., Indutnyi, F., Gasser, P.H., Münch, B., Wegmann, M. 2004. Three-
705 dimensional analysis of porous BaTiO3 ceramics using FIB nanotomography.
706 J. Microsc. 216 (1), 84-95.
707 Jarvis, P., Jefferson, B., Gregory, J., Parsons, S.A. 2005. A review of floc strength
708 and breakage. Water Res. 39 (14), 3121-3137.
709 Ketcham, R.A., Carlson, W.D. 2001. Acquisition, optimization and interpretation of X-
710 ray computed tomographic imagery: applications to the geosciences. Comput.
711 Geosci. 27, 381-400.
712 Khelifa, A. Hill, P.S. 2006. Models for effective density and settling velocity of flocs.
713 J. Hydraul. Res. 44, 390-401.
714 Lee, B.J., Toorman, E., Molz, F., Wang, J., 2011. A two-class population balance
715 equation yielding bimodal flocculation of marine or estuarine sediments. Water
716 Res. 45, 2131–2145.
717 Leppard, G.G. 1992. Size, morphology and composition of particulates in aquatic
718 ecosystems: solving speciation problems by correlative electron microscopy.
719 The Analyst 117 (3), 595-603.

Leppard, G.G., Heissenberger, A., Herndl, G.J. 1996. Ultrastructure of marine snow. I. Transmission electron microscopy methodology. Mar. Ecol. Prog. Ser. 135, 289-298.

Liss, S.N. 2002. Microbial Flocs Suspended Biofilms. In: Bitton, G. (Ed.), Encyclopaedia of Environmental Microbiology (Vol. 4). John Wiley and Sons, New York, NY, pp. 2000-2012.

Liss, S.N., Droppo, I.G., Flannigan, D.T., Leppard, G.G. 1996. Floc architecture in wastewater and natural riverine systems. Environ. Sci. Technol. 30 (2), 680-686.

Maggi, F., Mietta, F., Winterwerp, J.C. 2007. Effect of variable fractal dimension on the floc size distribution of suspended cohesive sediment. J. Hydrol. 343 (1-2), 43-55.

Manning, A.J., Dyer, K.R. 2002. The use of optics for the in situ determination of flocculated mud characteristics. J. Opt. A-Pure Appl. Op. 4, 71-81.

Nguyen, T.H., Tang, F.H., Maggi, F. 2017. Optical Measurement of cell Colonization Patterns on Individual Suspended Sediment aggregates. J. Geophys. Res. Earth Surf. 122 (10), 1794-1807.

Nguyen, T.P., Hankins, N.P., Hilal, N. 2007. A comparative study of the flocculation behaviour and final properties of synthetic and activated sludge in wastewater treatment. Desalination 204 (1), 277-295.

Ollion, J., Cochennec, J., Loll, F., Escudé, C., Boudier, T. 2013. TANGO: a generic tool for high-throughput 3D image analysis for studying nuclear organization. Bioinformatics 29, 1840-1841.

O’Shea, F.T., Cundy, A.B, Spencer, K.L. The contaminant legacy from historic coastal landfills and their potential as sourcse of diffuse pollution. Mar. Pollut. Bull. 128, 446-455.

Peachey, L.D. 1958. Thin Sections: I. A study of section thickness and physical distortion produced during microtomy. J. Biophys. Biochem. Cytol. 4 (3), 233-242.

Preibisch, S., Saalfeld, S., Tomancak, P. 2009. Globally optimal stitching of tiled 3D microscopic image acquisitions. Bioinformatics 25 (11), 1463-1465.

Righetti, M., Lucarelli, C. 2010. Resuspension phenomena of benthic sediments: the role of cohesion and biological adhesion. River Res. Appl. 26, 404-413.

Rummel, C.D., Jahnke, A., Gorokhova, E., Kühnel, D., Schmitt-Jansen, M. 2017. Impacts of Biofilm Formation on the Fate and Potential Effects of Microplastic in the Aquatic Environment. Environ. Sci. Technol. 4 (7), 258 - 267

Rusconi, R., Guasto, J. S., Stocker, R. 2014. Bacterial Transport Suppressed by Fluid Shear. Nat. Phys. 10 (3), 212−217.

Schindelin, J., Arganda-Carreras, I., Frise, E., Kaynig, V., Longair, M., Pietzsch, T., Preibisch, S., Rueden, C., Saalfeld, S., Schmid, B., Tinevez, J-Y., White, D. J., Hartenstein, V., Eliceiri, K., Tomancak, P., Cardona, A. 2012. Fiji: an open-source platform for biological-image analysis. Nature Methods 9 (7), 676-682.

Sharma, S., Lin, C-L., Miller, J.D. 2017. Multi-scale features including water content of polymer induced kaolinite floc structures. Miner. Eng. 101, 20-29.

Soulsby, R.L., Manning, A.J., Spearman, J., Whitehouse, R.J.S. 2013. Settling velocity and mass settling flux of flocculated estuarine sediments. Mar. Geol. 339, 1-12.

Tolhurst, T.J., Gust, G., Paterson, D.M. 2002. The influence on an extra-cellular polymeric substance (EPS) on cohesive sediment stability. In: Winterwerp, J.C., Kranenburg, C. (Eds.), Fine Sediment Dynamics in the Marine Environment - Proceedings in Marine Science 5. Elsevier Science, Amsterdam, pp. 409-425

Ward, A.K., Johnson, M.D. 1996. Heterotrophic microorganisms. In: Hauer, F.R., Lamberti, G.A. (Eds.), Methods in Stream Ecology. Academic Press, San Diego, CA, pp. 233-268.

Wheatland, J.A.T., Bushby, A.J., Spencer, K.L. 2017. Quantifying the structure and composition of flocculated suspended particulate matter using focused ion beam nanotomography. Environ. Sci. Technol. 51 (16), 8917-8925.

Winterwerp, J.C. 1998. A simple model for turbulence induced flocculation of cohesive sediment. J. Hyd. Eng. Res. 36 (3), 309-326.

Zhang, N., Thompson, C.E.L., Townend, I.H., Rankin, K.E., Paterson, D.M., Manning A.J. 2018. Nondestructive 3D imaging and quantification of hydrated biofilm-sediment aggregates using X‐ray microcomputed tomography. Environ. Sci. Technol. 52 (22), 13306-13313.

SUPPLEMENTARY FIGURES

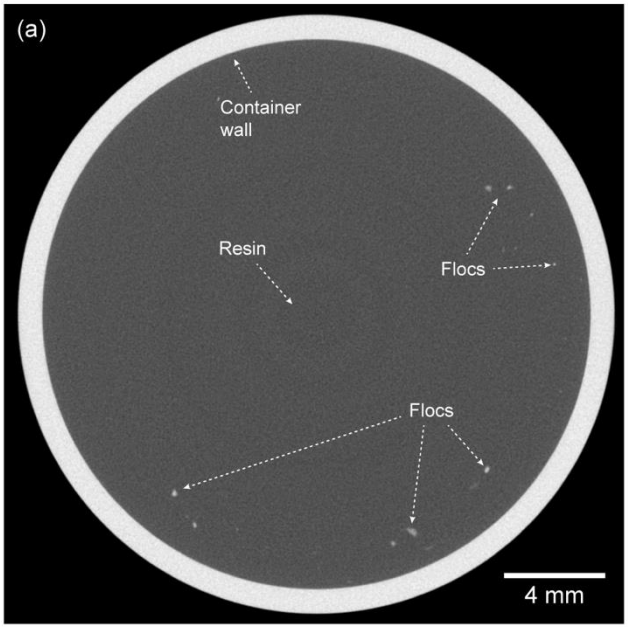

Supplementary Fig. S1. µCT cross-sectional image from the scan of test sample FS0, note the minimal overlap between neighbouring floc particles.

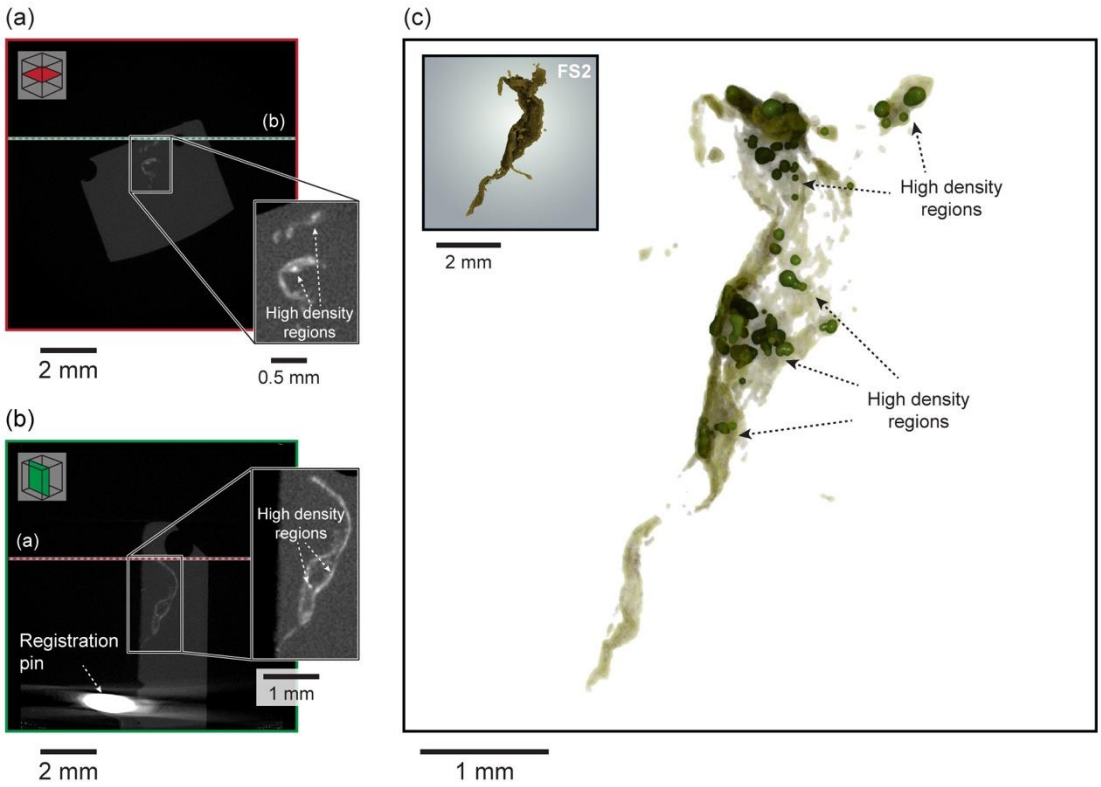

793

794 **Supplementary Fig. S2.** 3D visualisations of the floc samples FS2 (c). (a) and (b)

795 are image slices taken in two orthogonal planes from the µCT date; note the regions

796 of high and low X-ray attenuation within the floc shown in the magnified sub-sets; (c)

797 shows a 3D visualisation of floc FS2 but with the regions of low X-ray attenuation

798 rendered semi-transparent to reveal the regions of high attenuation.

799

800

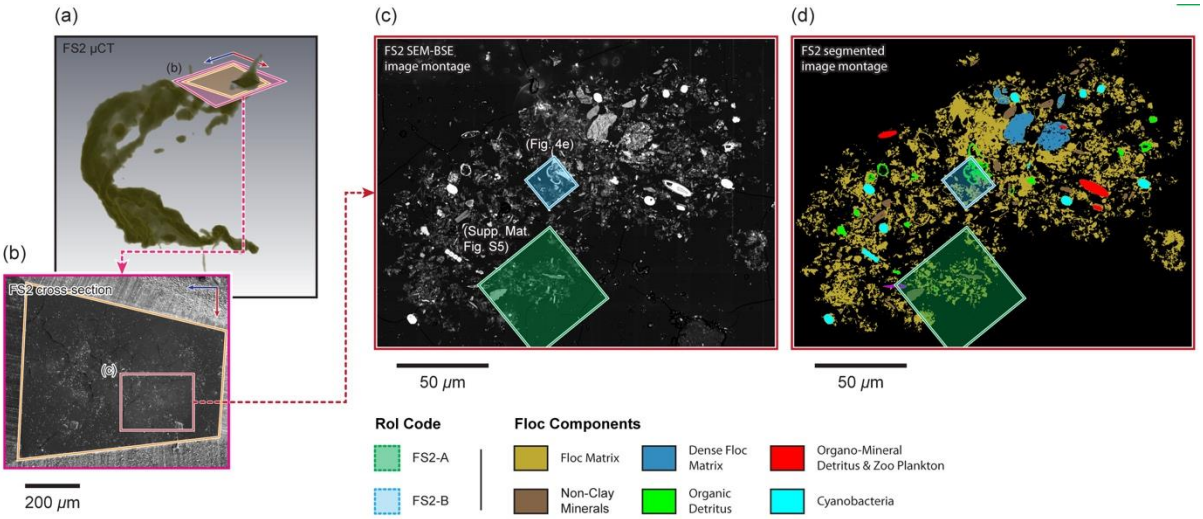

801

802 **Supplementary Fig. S3.** Analysis of the cross-section located in floc FS2. The
803 location of the cross-section created within FS2 is shown in (a) and the region of the
804 cross-section containing the floc is shown in (b). The trapezoidal shape of the
805 sectioned block is highlighted in orange both in (a) and (b), while the boundary of the
806 SEM image of the cross-section shown in (b) is defined in 3D space in (a) in pink.
807 The SEM-BSE image montage (c) obtained from the cross-section through floc FS2
808 enabled the identification of floc constituents (d) and characterisation of floc structure
809 in 2D. The locations of RoIs FS2-A and FS2-B selected for further analysis are
810 shown in (c) and (d).

811

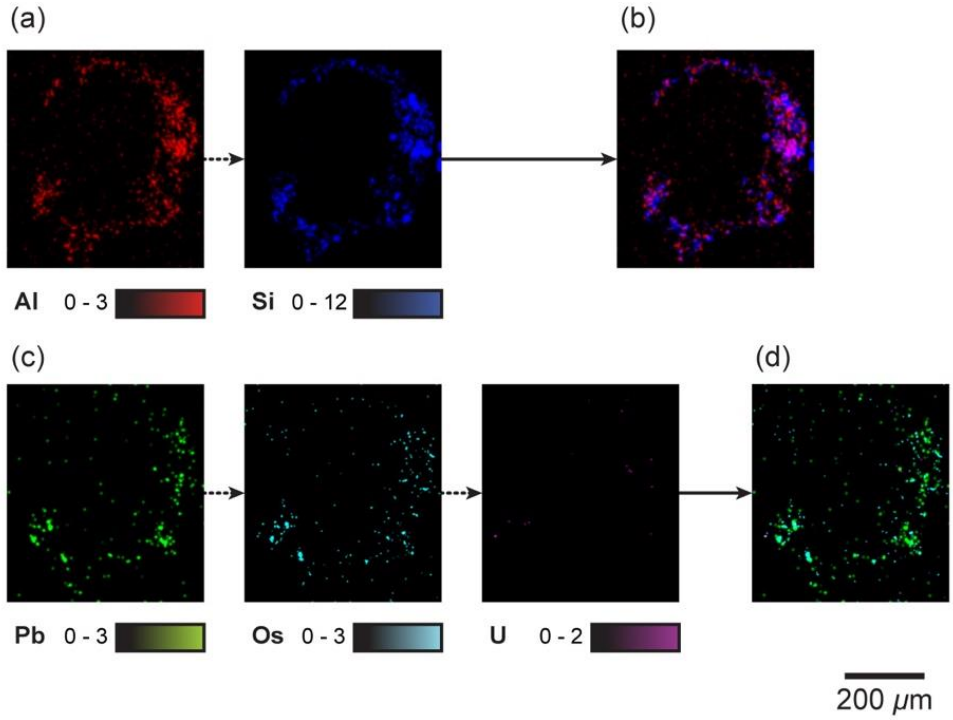

812

813 **Supplementary Fig. S4.** Individual SEM-EDS elemental maps collected from the

814 cross-section through floc FS2. (a) Inorganic signals for Al and Si; (b) combined

815 signal (phase map) for Al and Si; (c) Organic signals for Pb, Os, and U; (d) combined

816 signal for Pb, Os, and U.

817

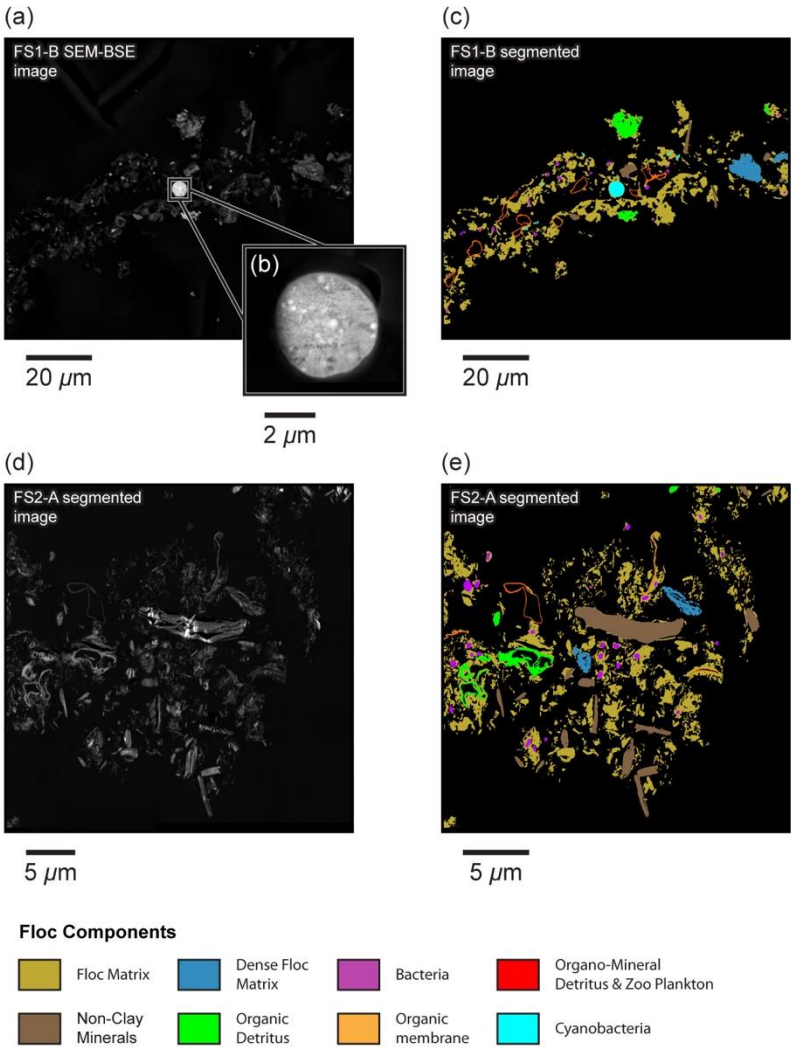

818

819 **Supplementary Fig. S5.** Characterisation of floc sub-micrometre composition and
820 structure in 2D within RoI FS1-B (a) and FS2-A (c). The locations of RoIs FS1-B and
821 FS2-A are shown in Fig. 3c and Fig. S4 of Supplementary Materials respectively. (b)
822 shows a magnified subset from (a) that isolates a single cyanobacteria to
823 demonstrates how differential staining of subcellular structures has taken place.

824

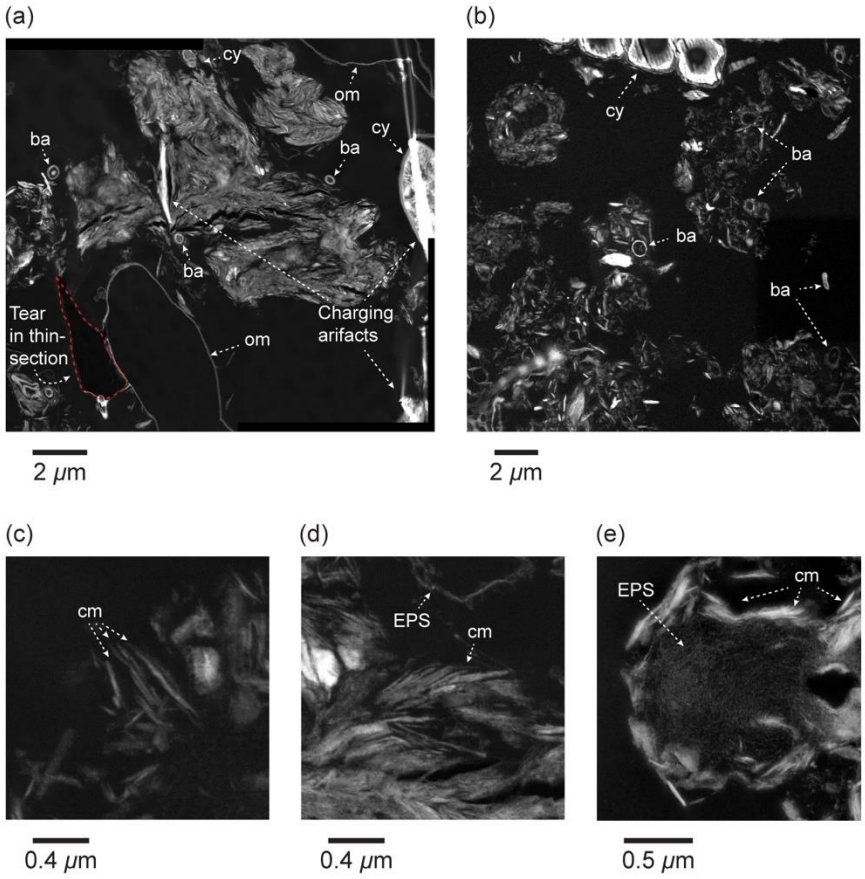

825

826 **Supplementary Fig. S6.** Selected STEM images illustrating the materials and
827 structures commonly observed within flocs FS1 and FS2. Regions of high and low
828 (clay) particle occupation are shown in (a) and (b) respectively. Note that regions of
829 high occupation primarily consisted of clay minerals aligned face-to-face, whereas
830 low occupation regions contained a variety of materials (e.g., clays, decaying organic
831 detritus, bacteria etc.). The high grey-scale values (c. >70) exhibited by units of high
832 occupation likely relates to clays coated in organic material in the nanometre range
833 filling the pore space between clay minerals. Regions of lower occupation were
834 commonly observed to consist of sub-units composed of clay platelets aligned face-
835 to-face and/or edge to face (c-d) and clay minerals arranged around a central
836 bacteria (see Fig. 5a). EPS can be observed filling the nm and μm pores within the
837 floc matrix (e).

838

Characterising the composition and multiscale structure of suspended sediment aggregates using 2D and 3D correlative microscopy

Highlights:

- Imaging workflow developed enabling multiscale floc properties to be explored for first time
- Correlative imaging enables visualisation and quantification of floc composition and structure
- Range of scale-dependent interactions observed that highlight the non-fractal nature of flocs

Development of novel 2D and 3D correlative microscopy to characterise the composition and multiscale structure of suspended sediment aggregates.

Jonathan A.T. Wheatland [a,b,c], Kate L. Spencer [c], Ian G. Droppo [d], Simon J. Carr [c,e] Andrew J. Bushby[a,b,*]

[a] School of Engineering & Materials Science, Queen Mary University of London, Mile End Road, London E1 4NS, UK

[b] The NanoVision Centre, Queen Mary University of London, Mile End Road, London E1 4NS, UK

[c] School of Geography, Queen Mary University of London, Mile End Road, London E1 4NS, UK

[d] Environment and Climate Change Canada, 867 Lakehouse Road, P.O. Box 5050, Burlington, Ontario L7S 1A1, Canada

[e] Department of Science, Natural Resources and Outdoor Studies, University of Cumbria, Ambleside, Cumbria LA22 8BB, UK

* Corresponding author. Email address: a.j.bushby@qmul.ac.uk

Abstract

Suspended cohesive sediments form aggregates or ‘flocs’ and are often closely associated with carbon, nutrients, pathogens and pollutants, which makes understanding their composition, transport and fate highly desirable. Accurate prediction of floc behaviour requires the quantification of 3-dimensional (3D) properties (size, shape and internal structure) that span several scales (i.e. nanometre [nm] to millimetre [mm]-scale). Traditional techniques (optical cameras and electron microscopy [EM]), however, can only provide 2-dimensional (2D)

simplifications of 3D floc geometries. Additionally, the existence of a resolution gap between conventional optical microscopy (COM) and transmission EM (TEM) prevents an understanding of how floc nm-scale constituents and internal structure influence mm-scale floc properties. Here, we develop a novel correlative imaging workflow combining 3D X-ray micro-computed tomography (µCT), 3D focused ion beam nanotomography (FIB-nt) and 2D scanning EM (SEM) and TEM (STEM) which allows us to stabilise, visualise and quantify the composition and multi-scale structure of sediment flocs for the first time. This new technique allowed the quantification of 3D floc geometries, the identification of individual floc components (e.g., clays, non-clay minerals and bacteria), and characterisation of particle-particle and structural associations across scales. This novel dataset demonstrates the truly complex structure of natural flocs at multiple scales. The integration of multi scale, state-of-the-art instrumentation/techniques offers the potential to generate fundamental new understanding of floc composition, structure and behaviour.

Keywords

Aquatic sediments, sediment aggregates, flocs, multiscale imaging, 2D and 3D correlative microscopy

1. Introduction

Cohesive fine-grained sediments and mixed sediments in suspension influence a wide array of environmental processes and material transfers, including the transport, fate and effect of carbon, nutrients, microbiota (including pathogens) and pollutants within lakes, rivers, estuaries and the marine environment (Azam & Long 2001; Rusconi et al. 2014; Rummel et al. 2017). Understanding the composition and behaviour of cohesive and mixed sediments is therefore a major issue for the

management of aquatic environments. However, in suspension this biotic and abiotic particulate matter forms loosely bound, complex and fragile aggregates, or ‘flocs’. Flocs exhibit hydrodynamics (e.g., transport dynamics and settling) that differ significantly from those of their constituent particles (Droppo 2001; Burd & Jackson 2009; Manning et al. 2010).

To predict the movement of cohesive sediments requires accurate quantification of floc properties that control their behaviour (e.g., size, shape, porosity and density) (Soulsby et al. 2013). Additionally, an understanding of floc composition and particle associations provides a mechanistic understanding of e.g., pathogen and pollutant transport and elucidates microbial dynamics (Liss 2002). Yet, obtaining such empirical data is challenging since flocs are inherently fragile and their properties often span several spatial scales, i.e. nm to mm-scale. Flocs are routinely characterised based on their ‘gross’ scale properties (e.g., external size and shape) that can be measured in situ relatively simply and non-destructively. Floc camera systems (e.g., LabSFLOC, Manning & Dyer 2002) and laser diffraction particle sizers (e.g., LISST, Agrawal & Pottsmith 2000) are commonly used and provide additional measurements of floc settling velocities. Internal floc characteristics (e.g., structure, density and porosity) cannot be measured directly using these methods, but can be estimated using Stokes’ Law and the assumption of spherical shape and fractal behaviour, i.e. structural self-similarity (Winterwerp 1998; Jarvis et al. 2005). Alternatively, sub-µm structures and the internal composition can be observed by, for instance, TEM (Leppard et al. 1996) or optical measurement of cell colonisation (e.g., Nguyen et al. 2017). However, there is no one method that allows floc structure and composition to be observed at all relevant spatial scales or that reflects the inherent 3D nature of these characteristics. A major challenge

therefore is the development of methods that enable empirical observation and accurate quantification of floc characteristics, correlated across multiple length-scales.

The combined application of two or more imaging methods, known as correlative microscopy, overcomes the resolution limitations associated with using a single imaging technique (Liss et al. 1996; Burnett et al. 2014). Previously, COM has been applied correlatively with confocal laser scanning microscopy (CLSM) and TEM enabling the investigation of floc mm-and nm-scale properties (Leppard 1992; Droppo et al. 1996; Liss et al. 1996; Leppard et al. 1996). Observations using this approach have provided valuable insights into floc structure-function relationships, highlighting the importance of floc-colonising microorganisms and their associated exopolymeric substances (EPS) (Droppo 2001; Tolhurst et al. 2002). However, the use of these imaging methods in a truly correlative manner is hindered by the specific preparation requirements, differences in contrast mechanisms, lack of overlap in resolution and their 2-dimensionality. Methods that can combine different spatial scales and similar contrast mechanisms with both 2D and 3D information are needed to understand delicate floc structures that include both organic and inorganic materials that extend across multiple scales. The combination of X-ray tomography with EM has the capability to achieve this across length-scales from mm to nm and the resolution gap can be closed. Furthermore, with similar sample preparation procedures, both imaging techniques can be applied to a single floc sample. Such methods have been used within materials science to visualise and quantify complex, multiscale structures from the cm to nm-scale (Handschuh et al. 2013; Burnett et al. 2014), and in the biological sciences (Bushby et al. 2012), but have not yet been applied to study natural environmental samples.

µCT and FIB-nt are both capable of imaging complex samples in 3D. µCT is capable of analysing volumes at a higher resolution than COM, and for small samples can reach a resolution of tens of µm down to submicrometre (Cnudde & Boone 2013). It is non-destructive and thus suited to imaging delicate samples, including sediments and hydrated, flocculated clays (e.g., Sharma et al. 2017; Zhang et al. 2018). FIB-nt is capable of resolutions approaching that of TEM (c. 10 nm, Holzer et al. 2004), and occupies a niche between TEM and µCT. Although FIB-nt is destructive, delicate samples can be stabilised to preserve their integrity during analysis (e.g., Bushby et al. 2011), and it has recently been successfully applied to investigate the internal structure of hydrated flocs (Wheatland et al. 2017). Significantly, both µCT and FIB-nt provide quantitative data (Holzer et al. 2004; Ketcham & Carlson 2001), which can be used to characterise suspended sediment flocs and potentially parameterise computational models that describe floc behaviour.

The aim of this study is to develop a correlative workflow that enables observation, characterisation and quantification of natural suspended sediment floc structure and composition from the mm to nm-scale for the first time. This workflow, which combines 3D µCT and FIB-nt with 2D SEM and STEM, is applied to the investigation of natural estuarine sediment flocs. Based on feature greyscale, size and morphology criteria are developed to distinguish floc components (e.g., clay minerals, bacteria etc.) observed at different spatial scales, which are used to segment the datasets.

2. Materials and Methods

2.1. Considerations for Correlative Imaging

Several challenges exist for the correlative imaging of sediment flocs. Firstly, fragile flocs must be sampled and stabilised and contrast agents (e.g., stains) applied to enable feature recognition using different imaging modalities operating at different scales (Wheatland et al. 2017). µCT and EM share similar contrast mechanisms allowing object(s) of interest to be identified and correlated between datasets. However, electron-dense stains must be introduced to allow organics to be distinguished. Secondly, to achieve correlation between the different imaging methods, datasets must be registered using fiducial markers that can be imaged by all methods. Thirdly, the process of identifying nm-scale datasets nested within mm-scale samples is represents a significant challenge (Bushby et al. 2011; Burnett et al. 2014). Therefore, workflows must follow a targeted approach whereby a sample is sequentially imaged at a finer scale and/or by a complimentary modality, the data from which is used to selected further regions of interest (RoI) for analysis at higher resolutions. Finally, the imaging methods used should each adequately resolve both the biotic and abiotic floc components for correlation. For example, µCT maps X-ray attenuation and hence images the density of an object or concentration of floc constituents at the µm to mm-scale. In comparison, SEM (using secondary and backscattered electrons) provides information on morphology and elemental composition at the nm to µm-scale. Combining this information enables important features (e.g., a pore space, clay mineral or bacteria) to be identified at different scales and resolutions. Once features have been identified, they can be segmented, quantified and visualised in both µCT and FIB-nt.

2.2. Floc Capture and Stabilisation

Natural sediment collected from the Thames Estuary, SE England. These sediments are typically fully saline, fine grained silty clays with organic content typically < 10% (measured as % loss on ignition, e.g., O'Shea et al. 2018). Sediment was added to an artificial seawater solution (Sigma sea salts 34 g L^{-1}) and gently agitated using a magnetic stirrer to induce flocculation. Fragile flocs were sampled following the protocol outlined in Droppo et al. (1996), which involved settling flocs directly into plankton chambers and immobilising flocs in agarose gel. µCT scans of a test sample (FS0, see Fig. S1 of Supplementary Materials) were conducted in order to assess potential artefacts associated with this technique (e.g., particle-particle overlap, Droppo et al. 1996). Immobilised flocs were subsequently prepared for imaging following the block staining protocol outlined in Wheatland et al. (2017). Floc samples were rendered vacuum stable by resin embedding, which included the addition of electron dense stains (e.g., uranyl acetate etc.) to improve the contrast of organic constituents. Following resin embedding, fiducial markers (aluminium wire, c. 0.5 mm diameter) were implanted in the base of each resin block for the purpose of data co-registration (see Section 2.3). Aluminium was selected as it could be easily distinguished from natural sedimentary material using all imaging methods (Handschuh et al. 2013).

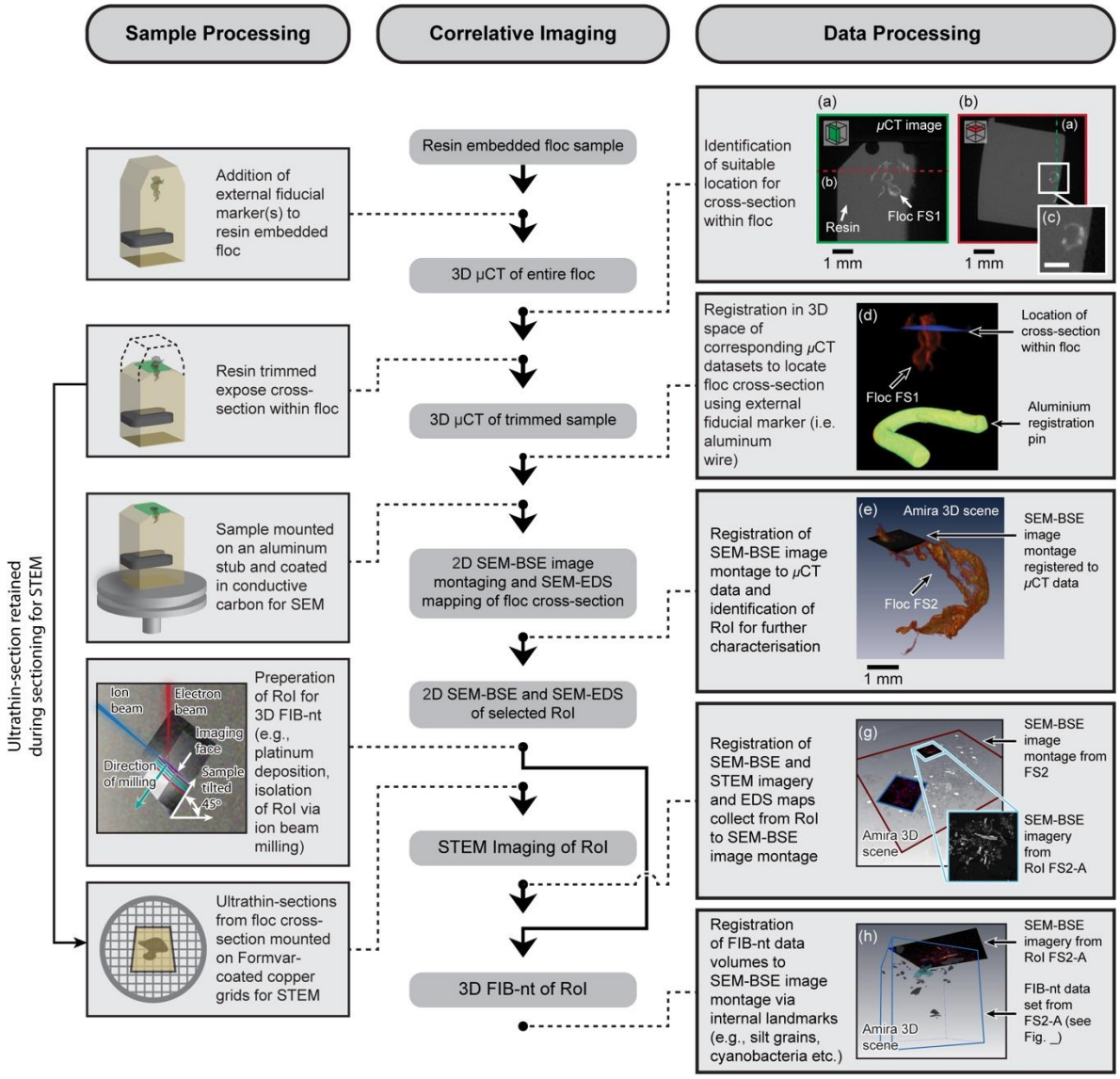

Figure 1. Flow diagram outlining the various stages in the correlative imaging workflow, including steps required for sample and data processing. Images (a) and (b) are orthogonal slices from the µCT scan of floc FS1. Grey-scale variations reflect regions of high and low X-ray attenuation (c), and indicate variability of floc constituents and structure at the sub-voxel scale. This information helps guide the selection of a suitable site for a cross-section within the floc which is exposed via ultramicrotomy. The precise location of the cross-section within the floc is then verified by re-scanning the sample using µCT and registering the two corresponding µCT datasets using the aluminium registration pin (d). 2D SEM-BSE image montages of the floc cross-section, obtained to identify suitable RoI for further analysis, are then registered to the µCT data (e). Following 2D SEM-BSE imaging, RoI are prepared for 3D FIB-nt (h). 2D SEM-BSE and STEM imagery and 3D FIB-nt data obtained from RoI can be registered to the image montage based on 'internal' fiducial markers (e.g., silt grains, cyanobacteria etc.) that can be identified in the corresponding datasets (g and h).

2.3. Description of the Correlative Workflow

The correlative workflow developed for investigating floc composition and multiscale structure is shown in Fig. 1. Low-resolution µCT scans (3D pixel or 'voxel' size, c. 10 μm^3) were initially conducted to characterise floc size and morphology and identify RoI for further analysis (Fig. 1a and b). At this resolution individual floc constituents <100 µm (e.g., bacteria and clay minerals) cannot be resolved. However, variations in X-ray attenuation (Fig. 1c and Fig. S2 of Supplementary Materials) indicate the variability of floc constituents and structure at the sub-voxel scale. Subsequently, selected RoIs were exposed by trimming the resin-block using an ultramicrotome (Leica UCT ultramicrotome), creating a smooth cross-section suitable for 2D SEM and 3D FIB-nt. During this process, ultrathin-sections (thickness, 70−100 nm) cut directly adjacent to the cross-section were retained for STEM (Fig. 1).

The accurate co-registration of µm and nm-scale EM datasets with mm-scale µCT scans relied on the location and characterisation of the cross-section created within the floc. Therefore, samples were re-scanned using µCT following ultramicrotomy to locate the floc cross-section within the original µCT data (Fig. 1d). This was facilitated by 'external' fiducial markers (aluminium wire) identifiable in the corresponding µCT datasets (Fig. 1d, see section 3.1.1). To ensure these repeat scans were directly comparable to the original µCT data and accurate co-registration, the position of the mechanical stage, manipulator settings (i.e. voltage and current) and resolution were kept constant.

2D SEM-BSE image montaging of the cross-section (block-face SEM) then provided the context within which to locate 3D FIB-nt volumes and 2D STEM imagery based on identification of 'internal' landmarks within the floc (Fig. 1g and h). Landmarks were selected that could be identified across scales and imaging

195 modalities, e.g., silt grains and cyanobacteria (see Table 1). Image montages were
196 obtained by systematic imaging using 2D SEM, resulting in 10's – 100's of images
197 that were stitched together to provide a 'panoramic' view of the entire cross-section
198 (pixel resolution, c. 100 nm^2). Following SEM imaging, elemental maps were
199 obtained from selected RoI via energy dispersive X-ray spectroscopy (SEM-EDS)
200 which, in conjunction with contrast and morphological information from SEM
201 imagery, enabled identification and mapping of materials.

202 2D SEM imagery and EDS maps informed the selection suitable sites for 3D
203 FIB-nt. Representativity is a key consideration when selecting parameters for FIB-nt
204 (i.e. volume size and resolution), and must be optimised to resolve features of
205 interest and ensure that a representative number of particles are characterised for
206 statistical analysis (Bushby et al. 2011). Natural flocs are compositionally complex,
207 containing particles of varying morphology and size (e.g., blocky silt grains, platy
208 clays, and filamentous organics), and high-resolution datasets are desirable (10-15
209 nm) to characterise individual particles. However, a trade-off must be made between
210 the resolution and volume size to ensure the µm-scale structures into which floc
211 constituents are organised are adequately characterised.

212

Imaging Technique; Successive Techniques Applied ⟶							
CT Datasets		SEM-BSE Montaging		SEM and STEM		FIB-nt	
Material	Identification Criteria	Material	Identification Criteria	Material	Identification Criteria	Material	Identification Criteria
Floc	Mid-range greyscale (c. 19,000 – 40,000) Variability in composition and structure at the sub-voxel scale	*Floc Matrix*	Material with diameter c. <10 µm, low to mid-range greyscales (c. 20 – 200) Regions of low and high occupation	*Clay Minerals*	2D planar morphology, size c. <5 µm, mid-range greyscale (c. 10 - 170)	*Clay minerals*	3D planar morphology, size c. <5 µm, mid-range greyscale (c. 10 - 170)
				Microbial Cells	Small size (c. <10 µm), high greyscale (c. 200 - 250),	*Cell Morpho-type*	Five cell morphotypes recognised based on

	recognised based on X-ray attenuation: low greyscale values (c. 25,000 – 40,000) correlated to regions of low-occupation, high greyscale values (c. 19,000 – 25,000) correlated to regions of high-occupation		identified based on greyscale, e.g., low occupation c. <50, high occupation c. >70		differential staining of subcellular structures		criteria outlined in Dazzo & Niccum (2015) (see Fig. 5)
						Intra-cellular Integrity	Three categories of intracellular integrity (indicative of metabolic state) recognised based on criteria outlined by Heissenberger et al. (1996) (see Fig. 5)
				Organo-Mineral Debris	Geometric structure, mid-range greyscale (c. 10 - 170)	*Organo-Mineral Debris*	Geometric structure, mid-range greyscale (c. 10 - 170)
				EPS	Fibrillar material, diameter (2 – 15 nm)	NA	
		Non-Clay Minerals	Blocky/ irregular morphology, particle size c. 5 – 40 µm, mid-range greyscales (c. 20 – 100)	*Non-Clay Minerals*	Blocky/ irregular morphology Particle size c. 5 – 40 µm, mid-range greyscales (c. 20 – 100)	*Non-Clay Minerals*	Blocky/ irregular morphology Particle size c. 5 – 40 µm, mid-range greyscales (c. 20 – 100)
		Bio-Organic Material	Irregularly shaped, high greyscales (c. 200 – 255)	*Bio-Organic Material*	Irregularly shaped, high greyscales (c. 200 – 255)	*Bio-Organic Material*	Irregularly shaped, high greyscales (c. 200 – 255)
Resin	Low greyscale (c. 7,000 – 17,000)	*Resin External to the Floc*	Resin external to the floc matrix, grey-scale (c. 0 – 20)	*Resin External to the Floc*	0 – 20	NA	
		Resin Filled Pore-Space	Resin filled pores within the floc matrix, low grey-scale (c. 0 – 20). NB only possible to resolve pores with diameter >30 µm	µm-Scale Pore	Resin filled pores within the floc matrix, low grey-scale (c. 0 – 20), diameter <10 µm	µm-Scale Pore	Resin filled pores within the floc matrix, low grey-scale (c. 0 – 20), diameter <10 µm
				nm-Scale Pores	Resin filled pores within the floc matrix, low grey-scale (c. 0 – 20), diameter >10 µm	nm-Scale Pores	Resin filled pores within the floc matrix, low grey-scale (c. 0 – 20), diameter >10 µm

Aluminium Pin	High greyscale (c. 45,000 – 65,535)	NA

Table 1. Materials identified within the various 2D and 3D datasets, and the criteria used for their identification/segmentation, e.g., size, morphology, and greyscale characteristics. Note, that the µCT are 16-bit and therefore have a pixel depth of 65,535 greyscales, whereas the SEM and STEM imagery and FIB-nt data volumes are 8-bit with a 256 greyscale range.

Ultrathin-sections collected adjacent to the surface of the cross-section during ultramicrotomy were mounted on Formvar-covered copper grids (Gilder Grids) and coated in conductive carbon for STEM. STEM provided details of the pore space that cannot be obtained using SEM. Additionally, high-resolution elemental analysis via STEM X-ray spectroscopy (STEM-EDS) conducted on floc cross-section (SEM-EDS) enabled the precise classification of individual floc constituents that cannot be achieved via SEM-EDS.

2.4. Acquisition of Image Data

2.4.1. 3D µCT

µCT scans were performed using a Nikon Metrology XT-H 225 (Tokyo, Japan) micro-tomograph. This scanner was configured with a 25-225 kV 0-2000 µA X-ray source with tungsten reflection target capable of generating polychromatic X-rays (focal spot size, c. 3 µm), and a Perkin Elmer (Waltham, Massachusetts, USA) 16-bit flat-panel detector. Scan parameters were set to optimise contrast and resolution (voltage 150 kV; current 160 µA; acquisition time between projections 2829 ms) with 2-frame averaging. Maintaining the same scan parameters for all µCT scans ensured comparability between datasets. The greyscale values of resulting

projections represented differences in X-ray energy attenuation, related to material density and the attenuation coefficient of the materials being imaged.

2.4.2. 2D SEM, STEM and EDS

2D SEM image montaging (block-face SEM) was conducted using an FIB-SEM (FEI Quanta 3D FEG, Hillsboro, Oregon, USA) fitted with a low-kV backscattered electron detector. Backscattered electron (BSE) images were collected at 3 kV accelerating voltage and 4 nA beam current to minimise the electron beam interaction volume and improve the spatial resolution of the BSE signal. Greyscale contrast of BSE images typically reflects composition. Systematic imaging of the floc cross-section generated 100's of images (pixel resolution, c. 30 – 60 nm^2). Images were subsequently stitched together into montages using the Grid/Collection Stitching plugin in open source software FIJI/ImageJ (Preibisch et al. 2009).

SEM-EDS elemental maps, STEM images and STEM-EDS point spectra were obtained using an FEI Inspect-F SEM fitted with a split field STEM detector (Hillsboro, Oregon, USA) and equipped with an Oxford Instruments (Oxford, UK) INCA X-act energy dispersive X-ray spectrometer. For low-resolution SEM-EDS mapping of the entire floc cross-section and high-resolution elemental mapping of RoI (see section 2.3) an accelerating voltage of 10 kV (counting period, 10 – 30 min). Counting periods varied between RoI and were selected to minimise damage to the sample surface. Dark-field STEM imaging of the ultrathin-sections was achieved at an accelerating voltage of 30 kV. Point spectra (STEM-EDS) were obtained from individual particles, at an accelerating voltage of 10 kV.

2.4.3. 3D FIB-nt Data Volumes

3D FIB-nt was performed using a FIB-SEM (FEI Quanta 3D FEG, Hillsboro, Oregon, USA) following the protocol outlined by Bushby et al. (2011). This relied on using the automated serial sectioning and imaging software Slice & View software (FEI Hillsboro, Oregon, USA). Experimentation revealed an accelerating voltage of 30 kV and a current of 0.5 – 5 nA for the ion beam to be optimal for milling. Images were captured using the BSE signal detector operated at a voltage of 3 kV and current of 4 nA, selected to match those used for 2D SEM (see section 2.4.2). The accuracy of FIB-nt relies on the stability of the FIB during milling and its ability to maintain regular intervals (i.e. slice thicknesses) between consecutive slices. An automated correction algorithm was applied during the serial sectioning procedure, which reduces or eliminates drift phenomena.

2.4.4. Reconstruction and Segmentation of the 3D Data

The product of µCT and FIB-nt are 2D projections/images of the sample/volume of interest that must be reconstructed to generate 3D volumes for visualisation and quantification. The reconstruction of µCT datasets was conducted using CTPro 3D (Nikon, Tokyo, Japan). Each scan generated 1,609 raw X-ray projections, yielding volumes with dimensions of 1,024 × 1,024 × 1,024 voxels (voxel size resolution, 10 μm^3). During reconstruction artefacts (e.g., beam hardening, Ketcham & Carlson 2001) were addressed by the application of specific algorithms. FIB-nt datasets were reconstructed following the protocol outlined by Bushby et al. (2011) using FIJI/ImageJ v2 (Schindelin et al. 2012). The number of images comprising FIB-nt datasets varied depending on the size of the analysed volume, ranging between 400

– 600 images. During setup for FIB-nt the mill thickness was adjusted to match the pixel resolution of the images, ensuring an isotropic voxel size suitable for quantitative analysis (Bushby et al. 2012).

2.4.5. Visualisation and Quantification of the Correlative Datasets

The quantification and visualisation of both µCT and FIB-nt datasets was conducted in in FIJI/ImageJ and required material segmentation, i.e. the classification of material phases based on greyscale values and/or shape, a critical stage in image processing (Cnudde & Boone 2013). Segmentation was achieved via greyscale thresholding or using a semi-automated segmentation tool plugin (Trainable WEKA Segmentation, TWS v2.1.0) capable of machine learning (Arganda-Carreras et al. 2017). The choice between these segmentation methods was guided by appraisal of dataset complexity, including the number of bulk phases and the overlap between phase greyscale envelopes common in natural environmental materials. Resulting binary volumes were then quantified using the 3DRoiManager plugin (Ollion et al. 2013), which provided quantitative measurements of material properties, e.g., size, shape and greyscale intensities etc.

2.4.6. Co-Registration of Datasets

The process of aligning multiscale datasets (i.e. co-registration) is a critical aspect of the correlative workflow, allowing information obtained using different imaging modalities and different spatial scales to be directly related. Co-registration of the multiscale 2D/3D datasets was achieved in the visualisation software Avizo (FEI Visualisation Sciences Group, Berlin, Germany). The success of registration is dependent upon the identification of fiducial markers in the different datasets. Co-

registration of µCT datasets relied upon the identification of the aluminium wire implanted within the resin block, whilst internal landmarks (e.g., silt particles, bacteria etc.) were used in the co-registration of higher resolution 2D and 3D datasets. Fig. 1 shows the sequence of steps taken to co-register the correlative datasets. Coarse alignment was manually conducted using the Transform Editor tool within Avizo, while fine registration was conducted automatically using the Landmark Surface Warp module applied using a rigid transformation algorithm.

3. Results and Discussion

3.1. Overview of the Multiscale Datasets

3.1.1. 3D Floc Sub-mm Structure and Internal Density

Volumetric renderings of three floc samples (FS1, FS2 and FS3) generated based on the µCT data (resolution, c. 10 μm^3) are shown in Fig. 2. For each 3D reconstruction greyscale contrast (16-bit pixel depth, e.g., 65,536 greyscales) between the flocs, surrounding resin and aluminium fiducial markers was sufficient to allow segmentation based on simple thresholding. This is illustrated in Fig. 1a and b that show cross-sectional greyscale images taken from the reconstructed µCT scan of FS1, in which the floc and surrounding resin are easily distinguishable. Scan parameters were kept constant for each of the flocs, and thus datasets are directly comparable. Table 1 details the criteria (e.g., greyscale range, size and shape etc.) for identify the different material phases; i) resin ii) floc, and iii) aluminium registration pin. The result of the segmentation procedure was a binary masks which formed the basis for subsequent visualisations and quantitative analysis (Fig. 2 and Table 2).

Quantitative analysis of the floc samples showed FS2 to have the largest volume, with a total occupied volume (i.e. voxel count) of 5.04×10^8 µm (Table 2).

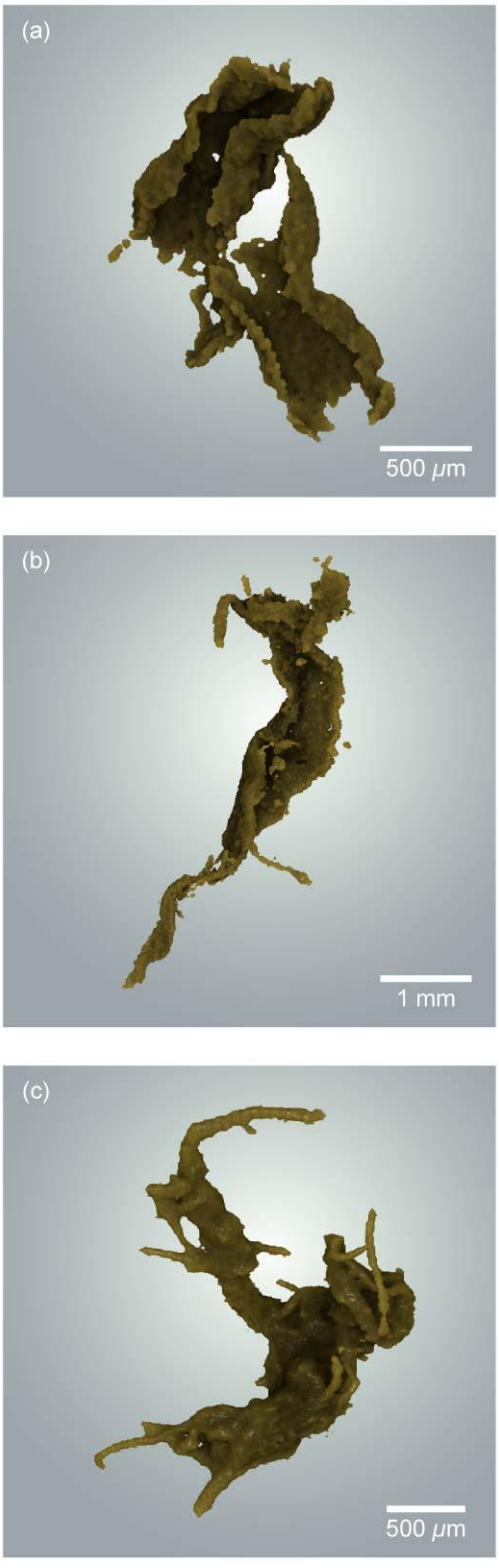

Figure 2. 3D visualisations of the floc samples FS1 (a) and FS2 (b) and FS3 (c) generated in Drishti from X-ray µCT data.

334 Descriptions of floc diameter (*D*) and height to width ratios (H/W) were made using
335 the Feret diameter, i.e. the distance between two parallel planes enclosing an object.

Based on these the floc samples can be described as macroflocs (*D*>160 µm; Manning & Dyer 2002) that exhibit elongate (H/W >2:1) and highly contorted morphologies. Flocs FS2 and FS3 exhibit filamentous protuberances projecting beyond their peripheries, likely related to the presence of cyanobacteria (confirmed by SEM, STEM and FIB-nt dataset, see sections 3.1.2, 3.1.3 and 3.1.4). FS1 was observed to differs significantly from FS2 and FS3, being composed of three distinct sub-units, connected by narrow linkages c. ≤30 µm. Each of the floc samples exhibited regions of high and low X- ray attenuation (Table 1 and Fig. 2c and Fig. S2 of Supplementary Materials). The distribution of regions of high attenuating elements within floc FS2 are shown in a 3D rendering in Fig. S2 of Supplementary Materials. This information provided a means of identifying RoI for further analysis (see Section 3.1.2 and Fig. 3a-c and Fig. S3 of Supplementary Materials).

Floc Sample	Floc Volume (μm^3)	Feret Diameter (µm)			H/W
		Major	Intermediate	Minor	
FS1	1.95×10^8	2414.54	1298.65	631.29	3:1
FS2	5.04×10^8	11183.83	755.82	266.06	4:1
FS3	2.44×10^8	945.03	800.19	323.23	2:1

Table 2. 3D quantitative measures of floc geometry (volume and Feret diameter) and shape (height/width ratio).

3.1.2. 2D Floc Micrometre-Structure and Composition Revealed in Cross-Section

Fig. 3c shows the 2D SEM-BSE image montage collected from the cross-section of floc FS1 (resolution, c. 60 nm^2), (FS2, resolution, c. 30 nm^2 and individual SEM-EDS

elemental maps are shown in Fig. S2 and Fig. S4 respectively). Similar to µCT, greyscale contrast (8-bit pixel depth, e.g., 256 greyscales) was sufficient to allow flocculated material to be segmented from surrounding resin. However, the higher resolution of SEM also enabled the recognition of additional floc components, which could be classified based on particle size, shape and greyscale value and further validated by comparison with SEM-EDS elemental maps. Four additional materials were identified; i) resin filled pore-space, ii) floc matrix (e.g., clays, unicellular bacteria, organo-mineral debris), iii) individual non-clay mineral grains (e.g., quartz, feldspar and mica) and iv) large bio-organic and organic structures (e.g., organic detritus, diatoms, cyanobacteria) (Table 1 and Fig. 3d). Particles <10 µm (e.g., EPS,

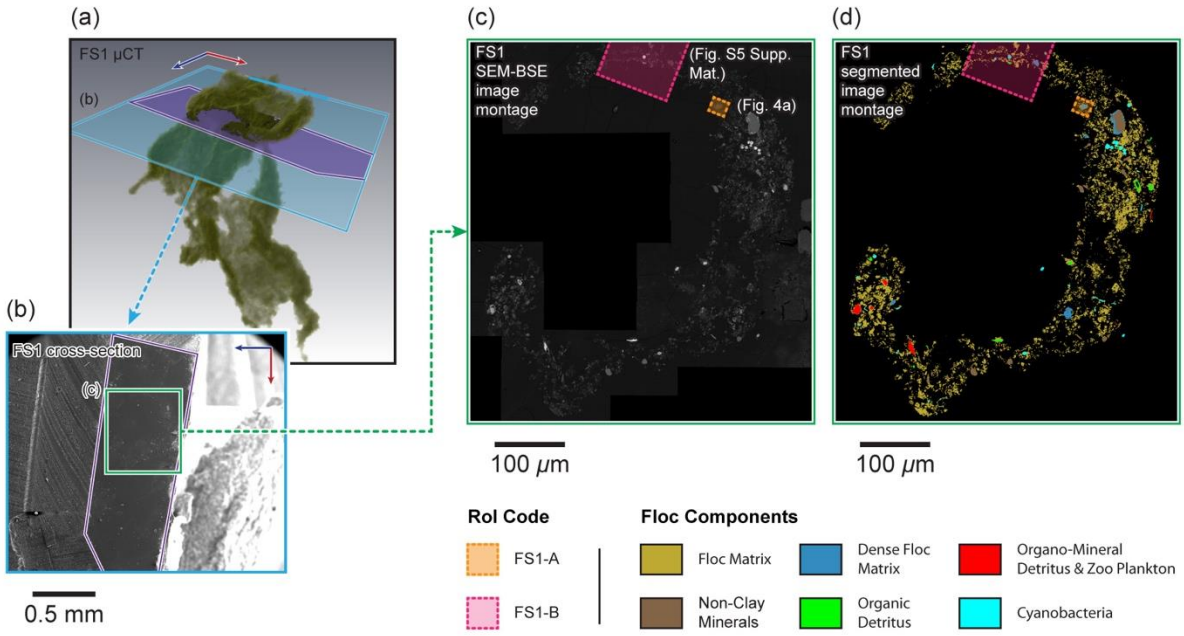

Figure 3. Analysis of the cross-section located in floc FS1. The location of the cross-section created within FS1 is shown in (a) and the region of the cross-section containing the floc is shown in (b). The trapezoidal shape of the sectioned block is highlighted in purple both in (a) and (b), while the boundary of the SEM image of the cross-section shown in (b) is defined in 3D space in (a) in blue. The SEM-BSE image montage (c) obtained from the cross-section through floc FS1 enabled the identification of floc constituents (d) and characterisation of floc structure in 2D. The locations of RoI selected for further analysis are shown in (c) and (d).

366 clay minerals and unicellular bacteria) could not be accurately segmented and were
367 identified collectively as ‘floc matrix’. The floc matrix is likely to be compositionally
368 complex, however, SEM-EDS revealed strong signals for Fe, Al/Si and Si (Fig. S4 of
369 Supplementary Materials), indicating the presence of iron oxyhydroxides, clay
370 minerals and silicates. Constituents were unevenly distributed within the floc matrix,
371 with regions of low occupation characterised by high porosity and low greyscale
372 values (c. <50) and regions of high occupation exhibiting low porosity and high
373 greyscale values (c. >70) (Fig. 3 and Table 1).

374 Non-clay mineral grains were differentiated based on their blocky/irregular
375 morphology, uniform greyscale and elemental signature (Si, Fe). In comparison, bio-
376 organic material and biota could be identified relatively easily based on their high
377 greyscale values (c. 200 – 255) due to heavy metal (Pb, Os and U) staining (see
378 also elemental phase map, Fig. S4 of Supplementary Materials). Strong signals for
379 Pb, Os and U related to heavy metal-stained organics, typically large features
380 (diameter, >10 µm) such as cyanobacteria and organic detritus, while an associated
381 signal of Si (blue) was indicative of eukaryotic plankton (e.g., diatom, foraminifera).

382

383 **3.1.3. 2D Submicrometre and Nanometre Structure and Composition of**
384 **Selected RoI**

385 For each floc several RoI were identified based on structural and/or compositional
386 characteristics revealed in SEM-BSE imagery and SEM-EDS elemental maps (see
387 Section 3.1.2). Fig. 3 and Fig. S3 of Supplementary Materials show the locations of
388 RoIs selected for FS1 and FS2 respectively. RoIs were targeted to either
389 characterise further floc nm composition and particle-particle interactions via STEM,

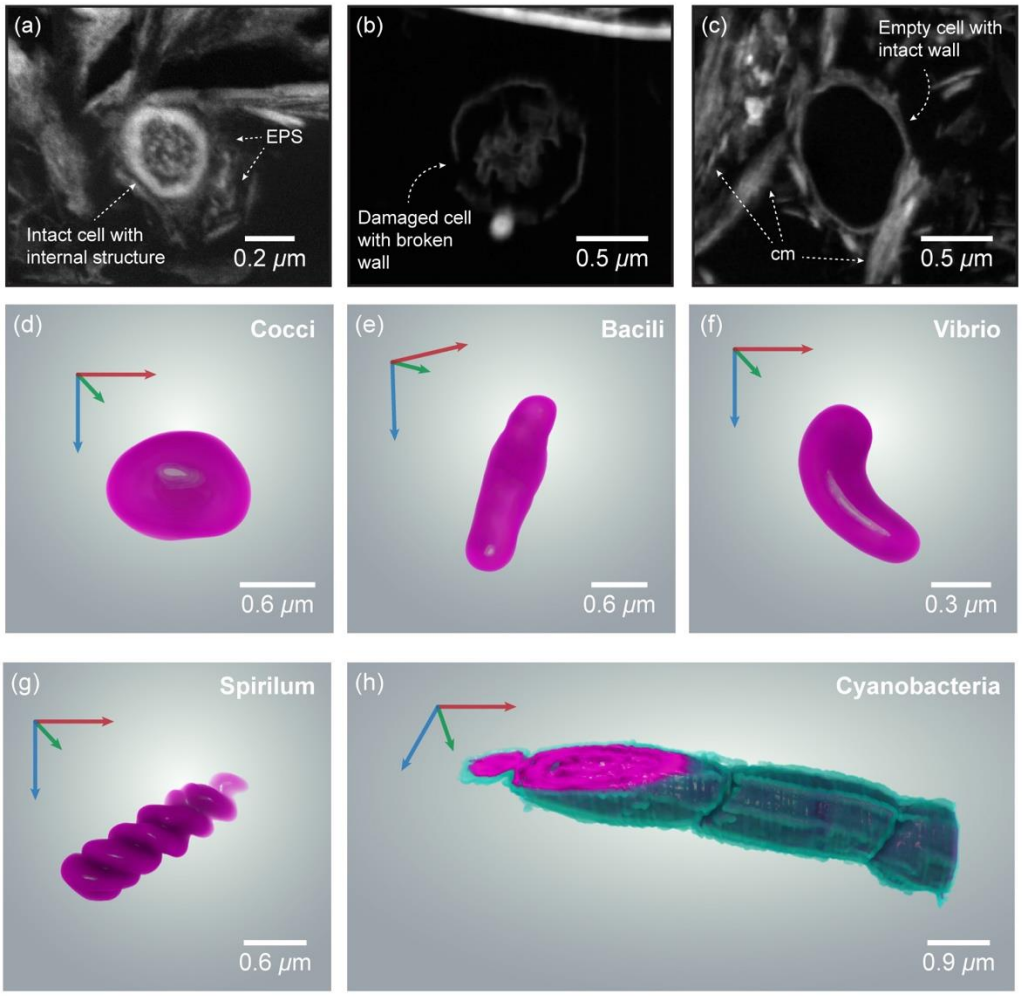

Figure 5. Characterisation of bacterial cells. (a – c) STEM images showing examples of the three categories of intracellular integrity used as an indicator of the fidelity of stabilised flocs to their original structure. (d – g) Examples of different bacterial cellular morphologies reconstructed based on 3D FIB-nt data. (a) intact bacteria displaying an undamaged cell wall, cytoplasm (grainy structure) and nucleoplasm (denser region towards the centre of the cell); (b) damaged bacterial cell with a broken cell wall and degraded cytoplasm and/or nucleoplasm; (c) empty cell lacking plasma. (d) cocci, (e) bacilli, (f) vibrio, (g) spirillum and (h) cyanobacteria.

or selected for SEM imaging to define submicrometre structure. Selected SEM-BSE (resolution, c. 25 - 30 nm^2) and STEM (resolution, c. 5 - 10 μm^2) imagery and corresponding SEM-EDS elemental maps are shown in Fig. 4 and Fig. S5 of Supplementary Materials.

394 The four main floc constituents (pore-space, floc matrix, non-clay mineral
395 grains, and large bioorganic and organic structures) were also identified in SEM-BSE
396 and STEM imagery. However, the higher resolution enabled further distinction
397 between materials within the floc matrix: i) clay minerals, ii) microbial cells, iii)
398 organo-mineral debris, and iv) EPS (Table 1). Microbial cells could be easily
399 identified due to their high greyscale values (c. >200) and differential staining of
400 subcellular structures (Fig. S5 of Supplementary Materials). High-resolution STEM
401 imagery revealed internal/external cell structure allowing the classification of
402 microbes based on their metabolic state (Heissenberger et al. 1996) as: i) intact, ii)
403 damaged and iii) empty (e.g., Fig. 5a – c). Whilst the resolution of SEM imagery
404 prevented the detection of EPS 2 – 20 nm in diameter (Leppard 1992), its presence
405 is confirmed by STEM imagery (Fig. S6 of Supplementary Materials). EPS was
406 observed to be closely associated or 'bound' to the cell walls of metabolically active
407 microbes, whilst 'soluble' EPS exuded by microorganisms was found throughout the
408 floc matrix and often associated with clay minerals (Fig. S6 of Supplementary
409 Materials).

410 To investigate density variations within the floc matrix (see Section 3.1.2, Fig.
411 3 and Figs. S3 and S4 of Supplementary Materials), RoIs FS1-A and FS2-B (Fig. 4a
412 and e) were selected to encompass regions exhibiting high and low occupation.
413 Within both high and low occupation regions clay minerals were rarely observed in
414 isolation, but were observed in units of 10's of particles. STEM imagery revealed
415 several common particle associations, including units of clay platelets aligned face-
416 to-face and/or edge to face, and clay minerals arranged around a central bacterium
417 (Fig. S6 of Supplementary Materials). Low density regions of the floc matrix mainly
418 consisted of particle associations arranged in open, 'card-house' structures, and

were highly porous (Fig. 4a). STEM showed the nanometre pore space between primary particles filled with exopolymeric material, whilst EPS was notably absent in the larger micrometre pore channels (Fig. S6 of Supplementary Materials). In comparison, high density areas consisted primarily of closely packed clay minerals dispersed with pyrite (Fe+S) (Fig. 4c), and had a lower porosity and high organic signal (Fig. 4d).

3.1.4. 3D Submicrometre-Structure and Composition of Selected RoI

Volumetric renderings of two FIB-nt volumes obtained from FS2, labelled FS2-A and FS2-B and corresponding to the RoI of the same name (see Fig. 4e and Fig. S5 of Supplementary Materials), are shown in Figs. 6 and 7 respectively. The large volume size of FS2-A (c. 8×10^4 μm^3, voxel size c. 67 nm) enabled the organisation of large submicrometre structures to be revealed in 3D, while the higher resolution of FS2-B (c. 5×10^3 μm^3, voxel size c. 15 nm) allowed for the detailed characterisation of constituents and particle-particle associations.

FIB-nt datasets were segmented following Wheatland et al. (2017). The primary floc constituents (resin filled pore-space, floc matrix, non-clay minerals, and large bioorganic and organic structures) and floc matrix constituents (clays minerals, microbial cells and organo-mineral debris) identified in 2D SEM and STEM were also identified in FIB-nt (Table 1 and Fig. 6 and 7). Additionally, the enhanced spatial resolution of FS2-B enabled the segmentation of closely packed particles c. <2 µm (e.g., clays within the floc matrix), enabling their reconstruction in 3D (Fig. 7e). This is demonstrated in Fig. 7d in which individual clays can be discriminated in 2D slices from the FIB-nt dataset. Several of the particle-particle associations identified within SEM and STEM data (see Section 3.1.3 and Fig. S6 of Supplementary Materials)

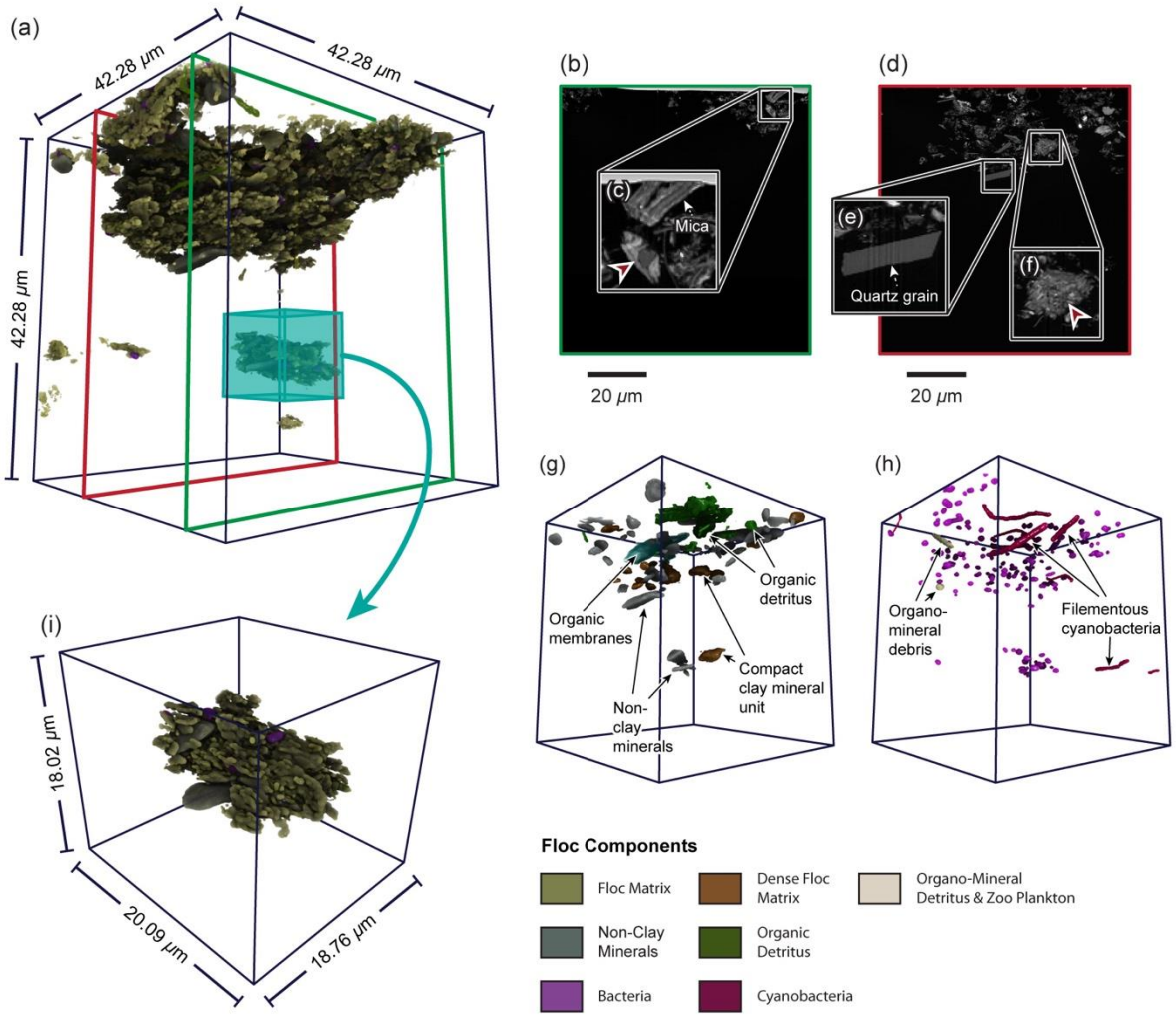

Figure 6. 3D reconstructions of the FIB-nt volume RoI FS2-A: (a) 3D rendering of the segmented components identified within FS2-A; (b - c) Selected BSE images from the FIB-nt dataset illustrating the differences in grey-scale and morphology that enable feature segmentation, note the red arrow shown in (c) highlights a region of high particle occupation. The locations from which the 2D BSE images shown in (b) and (c) were taken from within the FIB-nt dataset are indicated by coloured lines shown in (a); (g) Same as (a) but with selected materials rendered transparent to reveal the non-clay minerals, organic membranes and amorphous organic detritus; (h) Same as (a) but with certain materials rendered transparent to reveal the individual bacteria, cyanobacteria and organomineral debris (diatom frustules); e)) Sub-volume taken for FS2-A showing an isolated microfloc (location indicated in (a)).

were also identified in FS2-B. Visualised in 3D these structures are revealed to be discrete units, separable from surrounding floc matrix by nanopores (Fig. 7e and f).

Fig. 7e shows a particle association consisting of clay minerals aligned face-to-face, while Fig. 7f shows clay particles aligned around a central bacterium. Examination of the floc matrix reveals micrometre pore channels delineating the boundaries of discrete structural units 10's μm in diameter (e.g., Fig. 6i). These structures usually consist of several particle-particle associations and larger primary particles (e.g., silt grains, organic detritus), loosely arranged in an open, card-house structure, linked together by filamentous cyanobacteria.

Quantification reveals the occupied volume of FS2-A largely consists of inorganic material, with clays accounting for c. 98% of occupied space and non-clay minerals c. 0.5% (Table 3). In contrast, a larger proportion of FS2-B is occupied by organics, which accounted for c. 34% of the occupied volume compared to inorganic material, c. 66%. Within both FIB-nt datasets micrometre pore channels can be identified together with elongated nanopores throughout the floc matrix (Fig. 6 and 7). Combined, these give a total porosity of c. 95 % and c. 52 % for FS2-A and FS2-B respectively. The resolution and 3D nature of the datasets enabled the classification of microbial cells based on morphotype (Dazzo & Niccum 2015) and five categories were recognised: i) cocci, ii) regular straight rods (e.g., bacilli), iii) curved/U-rods (e.g., vibrio), iv) spirals (e.g., spirilla) and v) unbranched filaments (e.g., cyanobacteria) (Fig. 6d - h). Cocci were characterised as near spherical (length/width, <2:1) with diameters <1.5 μm (Fig. 6h), frequently forming groups of several cells. In comparison, bacilli exhibited a straight, rod-like morphology (length/width, <16:1) and were larger (diameter, c. 2 μm). Cells with a crescent curvature (comma-shaped) were identified as vibrio, and had similar dimensions to bacilli (Fig. 5d – h). Although observed less frequently, spirilla were classified as elongated cells displaying a distinctive repeated waveform (e.g., corkscrew-shaped).

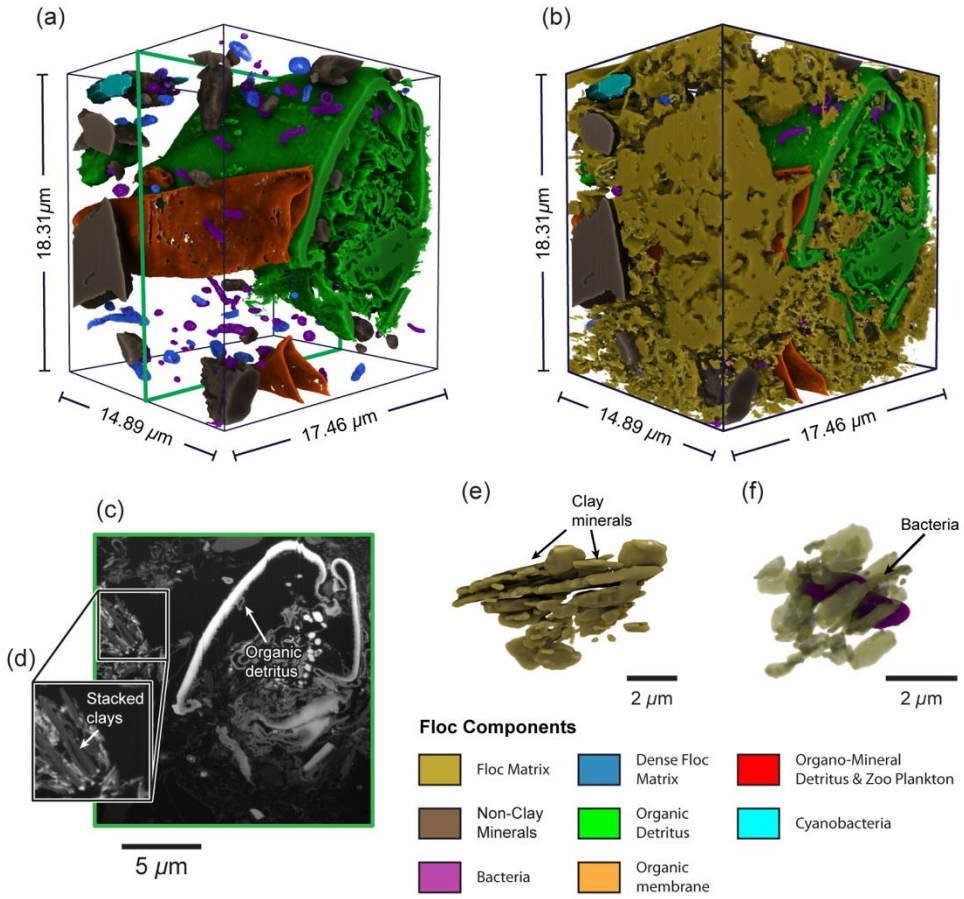

Figure 7. 3D reconstructions of the FIB-nt volume RoI FS2-B: (a) 3D rendering of the segmented components identified within FS2-B; (c) Selected BSE image from the FIB-nt dataset illustrating the differences in grey-scale and morphology that enable feature segmentation. The locations from which the 2D BSE image shown in (c) was taken from within the FIB-nt dataset are indicated by the green coloured line shown in (a); (d) Sub-set from (c) showing clay minerals aligned face-to-face and/or edge-to-face; (e) 3D reconstruction of (d); (f) Clay particle arranged radially around a bacterial cell (bacteria false-coloured purple).

Filamentous (cyanobacteria) bacteria could be easily distinguished from other cell types based on elongated shape (length/width, >16:1), and were present in a number of forms, ranging from cells 1 – 2 µm in diameter to larger varieties (diameters, c. >3 µm) (Fig. 5h). The quantities of cell morphotypes and their intracellular integrity (e.g., intact, damaged or empty, Heissenberger et al. 1996) are shown in Table 4.

FIB-nt Sample	Total Volume (μm^3)	Floc Constituents (Vol. %)						
		Porosity		Floc Matrix			Other	
		Micro-Porosity	Nano-Porosity	Clay Minerals	Bacteria	Organo-Mineral Debris	Organic Detritus	Non-Clay Minerals
FS2-A	c. 8×10^4	91.4	3.80	4.08	0.07	0.01	0.23	0.41
FS2-B	c. 5×10^3	-	51.79	31.96	0.45	0.07	17.16	2.15

Table 3. Volume fractions for the segmented components of FIB-nt datasets FS2-A and FS2-B.

FIB-nt Sample	Total Bacteria (Count)	Intracellular Integrity (% of Total Count)		Cell Morphotype (% of Total Count)				
		Intact Cells	Damaged and Empty Cells	Cocci	Regular Straight Rod	Curved/U-Rod	Unbranched Filament	Spiral
FS2-A	239	73.2	26.8	48.95	28.03	17.57	5.44	0
FS2-B	118	76.4	23.6	41.53	32.20	19.49	4.24	2.54

Table 4. Total count of bacteria, numbers of intact, damaged and empty cells and proportions of different cell morphotypes identified in FIB-nt datasets FS2-A and FS2-B.

3.2. Validation of Floc Stabilisation Method

Interpretation and quantification of 3D flocs relies on an assumption that the characteristics observed are representative of true floc structure and not artefacts of sampling, storage and preparation (Liss et al. 1996; Wheatland et al. 2017). The correlative workflow demonstrated above permits the validation of floc integrity in this context by enabling observation of 3D floc structure across multiple spatial scales.

Fluid exchanges and sample dehydration are essential for the chemical stabilisation process, but can result in the distortion and/or rupture of delicate cellular structures. While a number of cells identified in the 3D FIB-nt datasets were classified as either damaged or empty (Heissenberger et al. 1996) (Table 4), Wheatland et al. (2017) notes that the presence of damaged cells in itself is not indicative of inadequate stabilisation, since active microbial communities contain cells of all states of life including decay. More diagnostic of the state of preservation is the presence of intact cells, as rupture due to poor stabilisation would be expected to be systemic. Within the FIB-nt datasets intact cells accounted for c. >50% of the total number of cells, a higher percentage compared than that of the total number of metabolically active bacteria usually found in natural microbial communities (c. <30%, Ward & Johnson 1996). The loss of soluble EPS (i.e. EPS unassociated with bacterial cells) from the floc matrix during fluid exchanges can result in severe perturbation (Leppard et al. 1996). Previous studies have estimated up to 50−80% of EPS can be removed in certain instances from the floc matrix following stabilisation (Leppard et al. 1996), with the primary effect on the floc being the rearrangement of primary particles and compression of floc structures (recorded as shrinkage) (Liss et al. 1996). STEM imagery obtained from the floc samples reveals the presence of exopolymeric material, observed as dense networks in the nanometre pore space between primary particles (e.g., clays and bacteria) and distributed throughout the floc matrix (Fig. S6 of Supplementary Materials). This suggest that the little extraction of the EPS network within the floc matrix has taken place. The use of plankton chambers for floc capture and agarose gel for floc immobilisation help minimise the destructive forces associated with traditional sampling methods (e.g., floc breakage via pipetting) (Droppo et al. 1996). However, morphological changes

516 can result if flocs interact once settled, e.g., false aggregation of flocs and/or
517 pseudoplastic contortion of delicate structures with overburden pressure.
518 Examination of flocs of immobilised in agarose prior to resin embedding provides a
519 means of assessing the degree of interaction between neighbouring flocs. 2D cross-
520 sectional images taken from the µCT of test sample FS0 (Fig. S1 of Supplementary
521 Materials) reveal minimal overlap between neighbouring floc particles, suggesting
522 morphological changes to be minimal. This is supported by the 3D visualisation of
523 individual flocs (FS1, FS2 and FS3, Fig. 3 and Movie 1) that indicate delicate
524 structures (e.g., filamentous protuberances, Fig. 3b and c) remained intact following
525 settling and during the addition of agarose and sub-sampling for stabilisation.
526

527 **3.3. Merits of the Correlative Workflow**

528 This imaging workflow enables for the first time floc composition and 3D structure to
529 be investigated at all relevant spatial scales, from primary particles to entire flocs
530 several mm in size. This represents a significant advance in our ability to
531 characterise flocs, filling the resolution gap between traditional imaging techniques
532 (e.g., TEM, CLSM and COM) (Fig. 8).

533 The success of the workflow critically depends upon the quality (i.e. resolution,
534 signal-to-noise ratio) and degree of similarity (i.e. resolution and mechanisms for
535 contrast generation) between the different datasets (Caplan et al. 2011; Handschuh
536 et al. 2013). Image quality is of particular importance, since it determines the
537 accuracy with which features can be identified, segmented and quantified. Within
538 µCT and EM datasets the boundaries between objects are not always well defined,
539 but can consist of a transitional zone 3 – 5 pixels wide (Holzer et al. 2014;
540 Wheatland et a. 2017). Depending on the pixel/voxel resolution of the dataset the

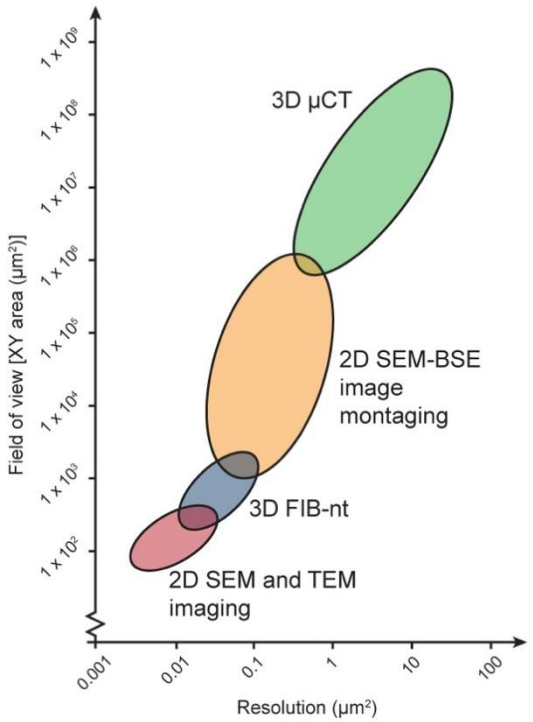

Figure 8. Length-scales over which the 2D and 3D imaging techniques employed within correlative workflow operate, with corresponding typical cross-section (XY) and resolution achievable by each technique. Note that the imaging methods used overlap, enabling truly correlative examination of floc structure from the nm to mm-scale.

maximum error is usually considered to be half the width of this zone. Further discussion regarding the process of segmentation and potential errors is outlined in Wheatland et al. (2017).

Fig. 3 shows the correlative 2D and 3D datasets collected from FS1 registered in a single 3D scene. To locate the floc cross-section, aluminium wire was used as a fiducial marker to register the µCT data collected after ultramicrotomy to the original µCT dataset of the intact flocs (see Section 2.3 and Fig. 1d). Segmentation of the

548 aluminium wire would ideally result in it being represented by similar number voxels

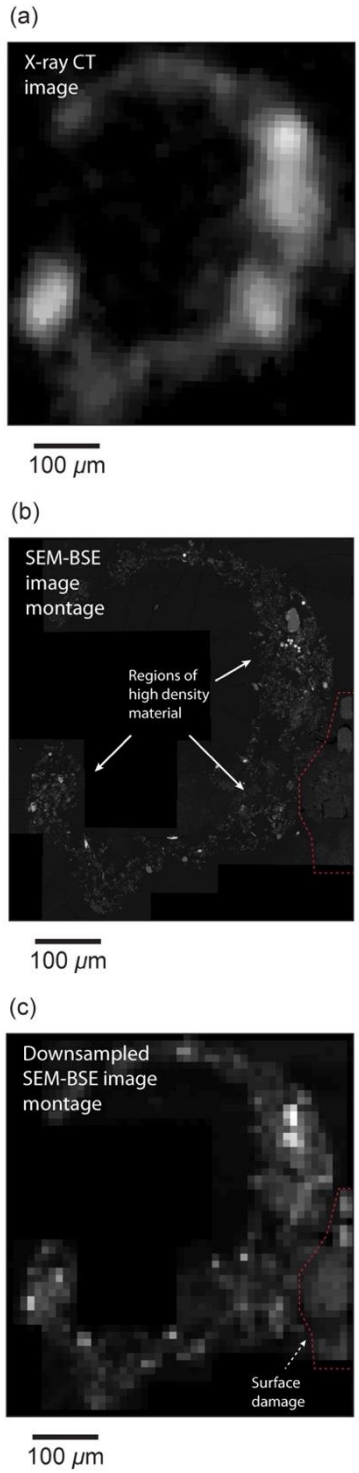

Figure 9. Comparison of µCT with SEM-BSE. Down-sampling the pixel size of the SEM-BSE image montage (c) to match that of the µCT data (c. 10 µm), enabled comparison between the SEM-BSE image montage (b) and corresponding µCT slice (a). This provides a means of validating the potential floc structures responsible for different greyscale values within the µCT dataset. Regions of the floc observed to contain high concentrations highlighted in (b) of particles in the BSE-SEM image montages were shown to exhibit high grey-scale values in the µCT dataset (a).

549 in the corresponding µCT datasets. Within both pairs of µCT data the wire was easily
550 segmented from other material phases based on its high greyscales (e.g., see
551 Section 3.1.1 and Fig. 2). However, discrepancies in the size of the segmented
552 aluminium wire were observed – 1.6% for FS1 and 3.8% for FS2 – which likely
553 resulted from scan artefacts, i.e. secondary edge effects due to partial volume effect.
554 Assuming an even distribution of the extraneous voxels around the surface area of
555 the aluminium fiducial marker, the minimum offset between co-registered datasets
556 can be estimated to be of the order of less than a voxel (c. 3 – 6 µm) over a total 3D
557 size of 10×10^8 µm. With evidence of only minor peripheral misalignment of the
558 registered datasets, the co-registration of the 3D µCT scans has been successful.
559 2D SEM-BSE image montages of the floc cross-sections were critical for the
560 co-registration of 2D and 3D nm and µm datasets with the sub mm-scale 3D µCT
561 data. The trapezoidal shape of the cross-sections (Fig. 3b and Fig. S3 of
562 Supplementary Materials) can be defined in the µCT datasets, enabling the SEM-
563 BSE image montages to be tied to the surface within an accuracy of 3 – 6 voxels (c.
564 30 – 60 µm). However, further confidence in the accuracy of the co-registration can
565 be obtained by comparing the actual shape of the floc boundary depicted in the two
566 datasets. Reducing the pixel resolution of the SEM-BSE image montages (i.e. down-
567 sampling) to match that of the µCT datasets (c. 10 µm) enables a direct comparison
568 between the SEM-BSE image montages and µCT data (Fig. 9), which indicates the
569 error to be less than a voxel (c. <10 µm). In addition, the features responsible for the
570 variations observed in µCT greyscale values, that reflect the variability of floc
571 constituents and structure at the sub-voxel scale (representing the impact of partial
572 volume effects, cf. Ketcham & Carlson 2001), can be confirmed by comparing the
573 down-sampled SEM-BSE image montage with the corresponding µCT slice. Fig. 9

demonstrates that regions of the SEM-BSE image montage identified as containing high concentrations of particles correspond to regions of high attenuation (high greyscales) within µCT. The similar imaging conditions selected for both SEM-BSE imaging (montaging and imaging of RoI) and FIB-nt allowed reference landmarks within the corresponding datasets to be recognised with a high degree of certainty (20 – 60 nm). As the contrast mechanisms in both SEM-BSE and dark-field STEM are similar (related to atomic number) fiducial markers internal to the floc (e.g., silt grains and bacteria etc.) could be easily identified. However, inspection of the overlaid STEM images following co-registration with SEM imagery revealed discrepancies in the positions of these markers. These displacements are likely the result of ultramicrotomy, as shear stresses imposed during sectioning are known to cause thin-section compression (Peachey 1958).

3.4 Applications of 3D Floc Structural and Compositional Data

Providing such detailed 3D analysis of flocs is not readily applicable for field scale quantification of suspended sediment aggregates. However, this technique has the potential, through targeted experimental or field campaigns, to provide new understanding of floc composition and controls on floc characteristics and structures. For example, these datasets quantify 3D floc characteristics (e.g., size, shape and porosity) that are critical input parameters to cohesive sediment transport models.

Additionally, the datasets demonstrate the complex structural associations and particle-particle interactions found at different spatial scales and levels of aggregation. These are frequently hypothesised in the literature or inferred from 2D observations of gross floc characteristics (e.g., Maggi et al. 2007; Lee et al. 2011). These particle-particle associations reflect the materials present in suspension

599 during floc development and their interactions. Here, the particle associations
600 including clays oriented face-to-face and/or edge-to-face likely occur due to a
601 combination of electrochemical interactions (i.e. cohesion), and the additional
602 binding forces provided by organic materials resulting in bioflocculation, i.e. adhesion
603 (Liss et al. 1996; Righetti & Lucarelli 2010). Yet the short distances (10^1 to 10^3 nm)
604 over which these forces (cohesion and adhesion) operate mean that these structures
605 are clearly scale-dependent. Larger structural units consisting of several particle-
606 particle associations and individual primary particles (e.g., silt grains, amorphous
607 organic detritus etc.) were found throughout the floc samples. Therefore, this new
608 method could provide data to challenge or validate simplified descriptors of floc
609 structure e.g., self-similarity or fractal geometry (e.g., Khelifa & Hill 2006).
610 Our data also demonstrate and quantify the microbial associations with
611 flocculated material. For example, demonstrating the importance of cell morphotype
612 on floc shape and strength. Here, filamentous cyanobacteria cross-link smaller
613 structural units (observed in 2D SEM and 3D FIB-nt) promoting interactions between
614 these structural units and providing structural connectivity and flexibility (e.g.,
615 Nguyen et al. 2007). Their strongly elongate shape and propensity to align has a
616 strong influence on floc development, promoting the growth of non-spherical flocs.
617 Additionally, filaments extending from the periphery of the flocs provide anchor
618 points to facilitate floc growth through interactions with other flocs (Burger et al
619 2017).
620
621 **4. Conclusion**
622 The development of a novel correlative workflow provides datasets demonstrating
623 the complex composition and multiscale 3D structure of aquatic sediment flocs. This

work provides the most detailed floc structural analysis to date and provides the following specific advantages:

- 2D and 3D imaging techniques can be applied in a systematic manner to successfully obtain a complete set of overlapping, co-registered datasets from a single floc sample. The resultant datasets enable the identification and quantification of floc composition and structures across multiple length-scales. This approach improves on traditional 2D correlative microscopy by providing truly correlative datasets that are quantifiable.
- The orientation of multi-scale and multi-modal datasets in 3D space presents a significant challenge, but can be successfully overcome using fiducial markers. This is reliant on selecting imaging techniques that share similar contrast mechanisms, to ensure that landmark features can be detected at different spatial scales.
- Particle-particle and structural associations can be directly related across length-scales. Structures that are scale-dependent can be recognised, providing further evidence for interactions that have previously been hypothesised. The imaging workflow therefore provides a means of obtaining quantitative measures of floc composition and structure and a better understanding of the mechanisms promoting floc growth.
- The correlative workflow is adaptable, and the potential exists for further research to design targeted experiments to explore relationships between floc structure and behaviour, controls on floc stability and structure, and floc microbial communities.

Acknowledgements

J.A.T.W. would like to thank the Engineering and Physical Sciences Research Council for the award of a scholarship and the Queen Mary University of London Postgraduate Research Fund. K.L.S, A.J.B and S.J.C acknowledge the Natural Environmental Research Council (NE/N011678/1) for funding. Jemima Burden (MRC Laboratory for Molecular Cell Biology, University College London) is thanked for her help with sample preparation.

References

Agrawal, Y.C., Pottsmith, H.C. 2000. Instruments for particle size and settling velocity observations in sediment transport. Mar. Geol. 168 (1–4), 89-114.

Arganda-Carreras, I., Kaynig, V., Rueden, C., Eliceiri, K.W., Schindelin, J., Cardona, A., Seung, H.S. 2017. Trainable Weka Segmentation: a machine learning tool for microscopy pixel classification. Bioinformatics 33 (15), 2424-2426.

Azam, F., Long, R.A. 2001. Sea snow microcosms. Nature 414, 495-498.

Burd, A.B. Jackson, G.A. 2009. Particle aggregation. Annu. Rev. Mar. Sci. 1, 65-90.

Burger, W., Krysiak-Baltyn, K., Scales, P.J., Martin, G.J.O., Stickland, A.D., Gras, S.L. 2017. The influence of protruding filamentous bacteria on floc stability and solid-liquid separation in the activated sludge process. Water Res. 123, 578-585.

Burnett, T.L., McDonald, S.A., Gholinia, A., Geurts, R., Janus, M., Slater, T., Haigh, S.J., Ornek, C., Almuaili, F., Engelberg, D.L., Thompson, G.E., Withers, P.J. 2014. Correlative tomography. Sci. Rep. 4, 1-6.

672 Bushby, A.J., Png, K.M.Y., Young, R.D., Pinali, C., Knupp C., Quantock A.J. 2011.
673 imaging three-dimensional tissue architectures by focused ion beam scanning
674 electron microscopy. Nat. Protoc. 6 (6), 845-858.
675 Bushby, A.J., Mariggi, G., Armer, H.E.J., Collinson, L.M. 2012. Correlative Light and
676 Volume EM: Using Focused Ion Beam Scanning Electron Microscopy to image
677 transient events in model organisms. Methods Cell Biol. 111, 357-382.
678 Caplan, J., Niethammer, M., Taylor, R.M., Czymmek, K.J. 2011. The power of
679 correlative microscopy: multi-modal, multi-scale, multi-dimensional. Curr. Opin.
680 Struct. Biol. 21 (5), 686-693.
681 Cnudde, V., Boone, M.N. 2013. High-resolution X-ray computed tomography in
682 geosciences: A review of the current technology and applications. Earth-Sci.
683 Rev. 23, 1-17.
684 Dazzo F.B., Niccum, B.C. 2015. Use of CMEIAS image analysis software to
685 accurately compute attributes of cell size, morphology, spatial aggregation and
686 color segmentation that signify in situ ecophysiological adaptations in microbial
687 biofilm communities. Computation 3, 72-98.
688 Droppo, I.G. 2001. Rethinking what constitutes suspended sediments. Hydrol.
689 Process. 15 (9), 1551-1564.
690 Droppo, I.G. 2003. A new definition of suspended sediment: implications for the
691 measurement and prediction of sediment transport. In: Bogen, J., Fergus, T.,
692 Walling, D. (Eds.), Erosion and Sediment Transport Measurement in Rivers:
693 Technological and Methodological Advances. IAHS Publication No. 249,
694 International Association of Hydrological Sciences, Wallinford, pp. 238.

695 Droppo, I.G., Flannigan, D.T., Leppard, G.G., Jaskot, C., Liss, S.N. 1996. Floc
696 stabilization for multiple microscopic techniques. Appl. Environ. Microbiol. 62,
697 3508-3515.
698 Handschuh, S., Baeumler, N., Schwaha, T., Ruthensteiner, B. 2013. A correlative
699 approach for combining microCT, light and transmission electron microscopy in
700 a single 3D scenario. Front. Zool. 10, 1-16.
701 Heissenberger A., Leppard, G.G., Herndl, G.J. 1996. Relationship between the
702 intracellular integrity and the morphology of the capsular envelope in attached
703 and free-living marine bacteria. Appl. Environ. Microbiol. 62 (12), 4521-4528.
704 Holzer, L., Indutnyi, F., Gasser, P.H., Münch, B., Wegmann, M. 2004. Three-
705 dimensional analysis of porous BaTiO3 ceramics using FIB nanotomography.
706 J. Microsc. 216 (1), 84-95.
707 Jarvis, P., Jefferson, B., Gregory, J., Parsons, S.A. 2005. A review of floc strength
708 and breakage. Water Res. 39 (14), 3121-3137.
709 Ketcham, R.A., Carlson, W.D. 2001. Acquisition, optimization and interpretation of X-
710 ray computed tomographic imagery: applications to the geosciences. Comput.
711 Geosci. 27, 381-400.
712 Khelifa, A. Hill, P.S. 2006. Models for effective density and settling velocity of flocs.
713 J. Hydraul. Res. 44, 390-401.
714 Lee, B.J., Toorman, E., Molz, F., Wang, J., 2011. A two-class population balance
715 equation yielding bimodal flocculation of marine or estuarine sediments. Water
716 Res. 45, 2131–2145.
717 Leppard, G.G. 1992. Size, morphology and composition of particulates in aquatic
718 ecosystems: solving speciation problems by correlative electron microscopy.
719 The Analyst 117 (3), 595-603.

Leppard, G.G., Heissenberger, A., Herndl, G.J. 1996. Ultrastructure of marine snow. I. Transmission electron microscopy methodology. Mar. Ecol. Prog. Ser. 135, 289-298.

Liss, S.N. 2002. Microbial Flocs Suspended Biofilms. In: Bitton, G. (Ed.), Encyclopaedia of Environmental Microbiology (Vol. 4). John Wiley and Sons, New York, NY, pp. 2000-2012.

Liss, S.N., Droppo, I.G., Flannigan, D.T., Leppard, G.G. 1996. Floc architecture in wastewater and natural riverine systems. Environ. Sci. Technol. 30 (2), 680-686.

Maggi, F., Mietta, F., Winterwerp, J.C. 2007. Effect of variable fractal dimension on the floc size distribution of suspended cohesive sediment. J. Hydrol. 343 (1-2), 43-55.

Manning, A.J., Dyer, K.R. 2002. The use of optics for the in situ determination of flocculated mud characteristics. J. Opt. A-Pure Appl. Op. 4, 71-81.

Nguyen, T.H., Tang, F.H., Maggi, F. 2017. Optical Measurement of cell Colonization Patterns on Individual Suspended Sediment aggregates. J. Geophys. Res. Earth Surf. 122 (10), 1794-1807.

Nguyen, T.P., Hankins, N.P., Hilal, N. 2007. A comparative study of the flocculation behaviour and final properties of synthetic and activated sludge in wastewater treatment. Desalination 204 (1), 277-295.

Ollion, J., Cochennec, J., Loll, F., Escudé, C., Boudier, T. 2013. TANGO: a generic tool for high-throughput 3D image analysis for studying nuclear organization. Bioinformatics 29, 1840-1841.

O’Shea, F.T., Cundy, A.B, Spencer, K.L. The contaminant legacy from historic coastal landfills and their potential as sourcse of diffuse pollution. Mar. Pollut. Bull. 128, 446-455.

Peachey, L.D. 1958. Thin Sections: I. A study of section thickness and physical distortion produced during microtomy. J. Biophys. Biochem. Cytol. 4 (3), 233-242.

Preibisch, S., Saalfeld, S., Tomancak, P. 2009. Globally optimal stitching of tiled 3D microscopic image acquisitions. Bioinformatics 25 (11), 1463-1465.

Righetti, M., Lucarelli, C. 2010. Resuspension phenomena of benthic sediments: the role of cohesion and biological adhesion. River Res. Appl. 26, 404-413.

Rummel, C.D., Jahnke, A., Gorokhova, E., Kühnel, D., Schmitt-Jansen, M. 2017. Impacts of Biofilm Formation on the Fate and Potential Effects of Microplastic in the Aquatic Environment. Environ. Sci. Technol. 4 (7), 258 - 267

Rusconi, R., Guasto, J. S., Stocker, R. 2014. Bacterial Transport Suppressed by Fluid Shear. Nat. Phys. 10 (3), 212−217.

Schindelin, J., Arganda-Carreras, I., Frise, E., Kaynig, V., Longair, M., Pietzsch, T., Preibisch, S., Rueden, C., Saalfeld, S., Schmid, B., Tinevez, J-Y., White, D. J., Hartenstein, V., Eliceiri, K., Tomancak, P., Cardona, A. 2012. Fiji: an open-source platform for biological-image analysis. Nature Methods 9 (7), 676-682.

Sharma, S., Lin, C-L., Miller, J.D. 2017. Multi-scale features including water content of polymer induced kaolinite floc structures. Miner. Eng. 101, 20-29.

Soulsby, R.L., Manning, A.J., Spearman, J., Whitehouse, R.J.S. 2013. Settling velocity and mass settling flux of flocculated estuarine sediments. Mar. Geol. 339, 1-12.

Tolhurst, T.J., Gust, G., Paterson, D.M. 2002. The influence on an extra-cellular polymeric substance (EPS) on cohesive sediment stability. In: Winterwerp, J.C., Kranenburg, C. (Eds.), Fine Sediment Dynamics in the Marine Environment - Proceedings in Marine Science 5. Elsevier Science, Amsterdam, pp. 409-425

Ward, A.K., Johnson, M.D. 1996. Heterotrophic microorganisms. In: Hauer, F.R., Lamberti, G.A. (Eds.), Methods in Stream Ecology. Academic Press, San Diego, CA, pp. 233-268.

Wheatland, J.A.T., Bushby, A.J., Spencer, K.L. 2017. Quantifying the structure and composition of flocculated suspended particulate matter using focused ion beam nanotomography. Environ. Sci. Technol. 51 (16), 8917-8925.

Winterwerp, J.C. 1998. A simple model for turbulence induced flocculation of cohesive sediment. J. Hyd. Eng. Res. 36 (3), 309-326.

Zhang, N., Thompson, C.E.L., Townend, I.H., Rankin, K.E., Paterson, D.M., Manning A.J. 2018. Nondestructive 3D imaging and quantification of hydrated biofilm-sediment aggregates using X‐ray microcomputed tomography. Environ. Sci. Technol. 52 (22), 13306-13313.

SUPPLEMENTARY FIGURES

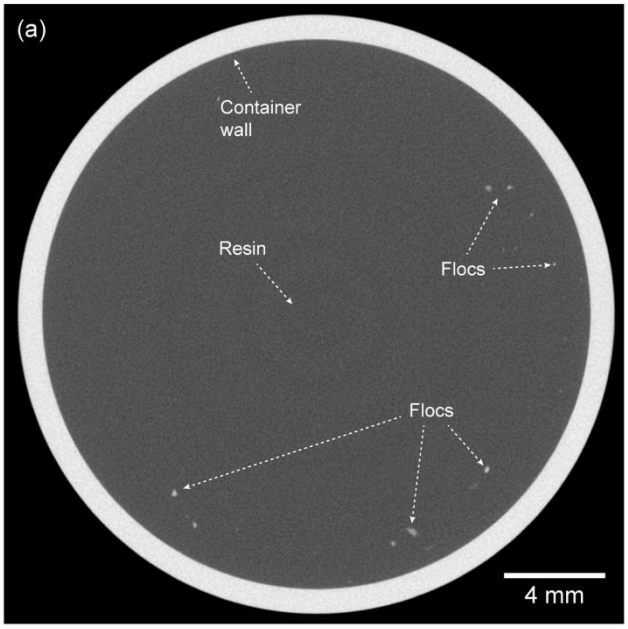

Supplementary Fig. S1. µCT cross-sectional image from the scan of test sample FS0, note the minimal overlap between neighbouring floc particles.

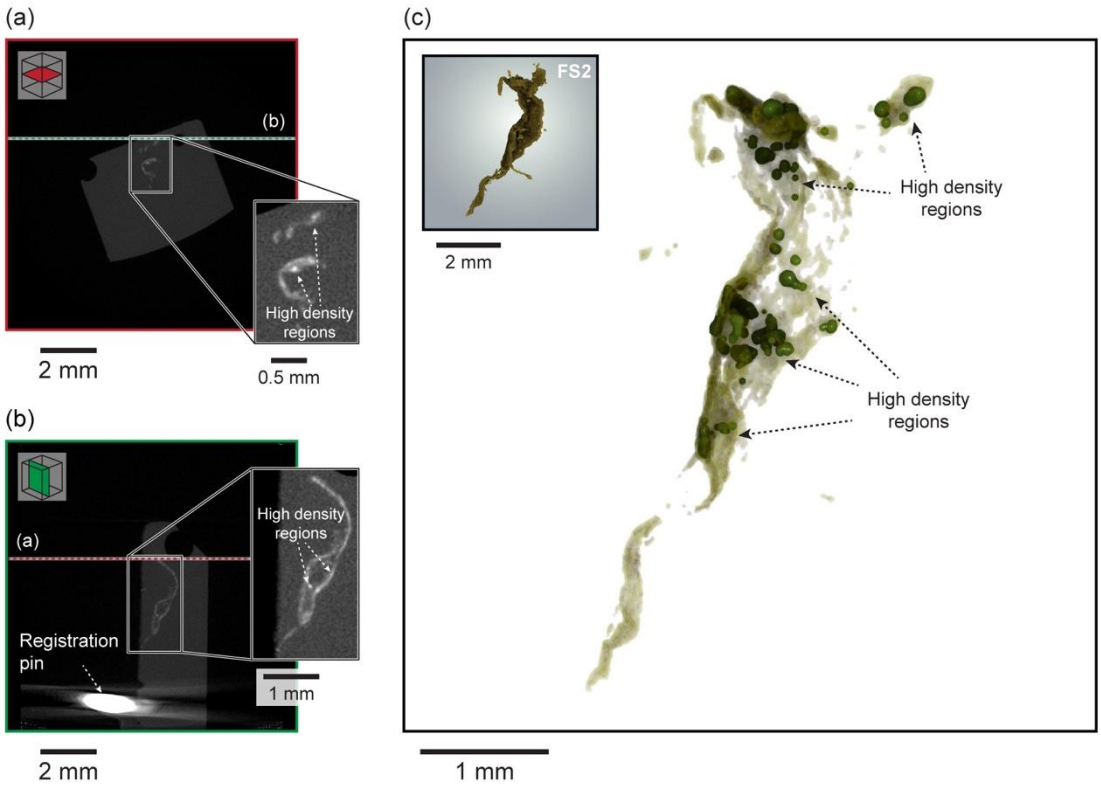

793

794 **Supplementary Fig. S2.** 3D visualisations of the floc samples FS2 (c). (a) and (b)

795 are image slices taken in two orthogonal planes from the µCT date; note the regions

796 of high and low X-ray attenuation within the floc shown in the magnified sub-sets; (c)

797 shows a 3D visualisation of floc FS2 but with the regions of low X-ray attenuation

798 rendered semi-transparent to reveal the regions of high attenuation.

799

800

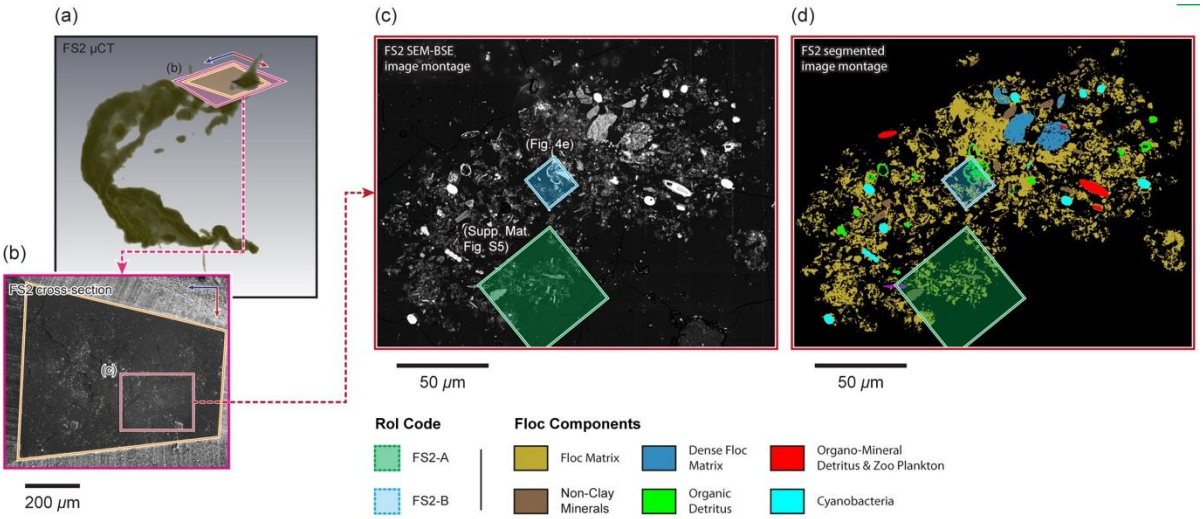

801

802 **Supplementary Fig. S3.** Analysis of the cross-section located in floc FS2. The
803 location of the cross-section created within FS2 is shown in (a) and the region of the
804 cross-section containing the floc is shown in (b). The trapezoidal shape of the
805 sectioned block is highlighted in orange both in (a) and (b), while the boundary of the
806 SEM image of the cross-section shown in (b) is defined in 3D space in (a) in pink.
807 The SEM-BSE image montage (c) obtained from the cross-section through floc FS2
808 enabled the identification of floc constituents (d) and characterisation of floc structure
809 in 2D. The locations of RoIs FS2-A and FS2-B selected for further analysis are
810 shown in (c) and (d).

811

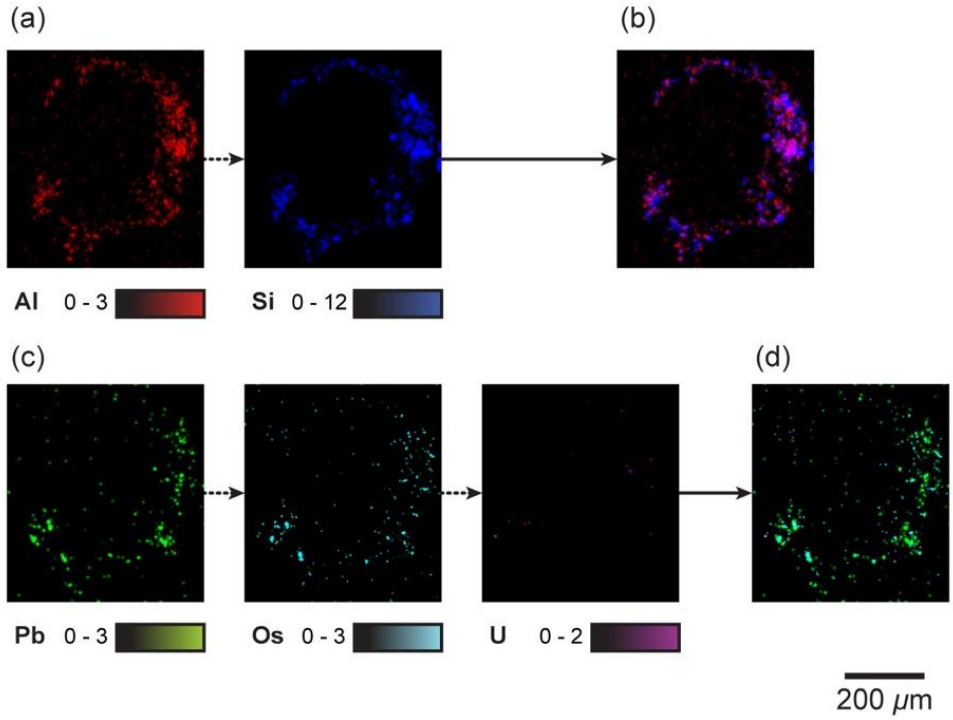

812

813 **Supplementary Fig. S4.** Individual SEM-EDS elemental maps collected from the

814 cross-section through floc FS2. (a) Inorganic signals for Al and Si; (b) combined

815 signal (phase map) for Al and Si; (c) Organic signals for Pb, Os, and U; (d) combined

816 signal for Pb, Os, and U.

817

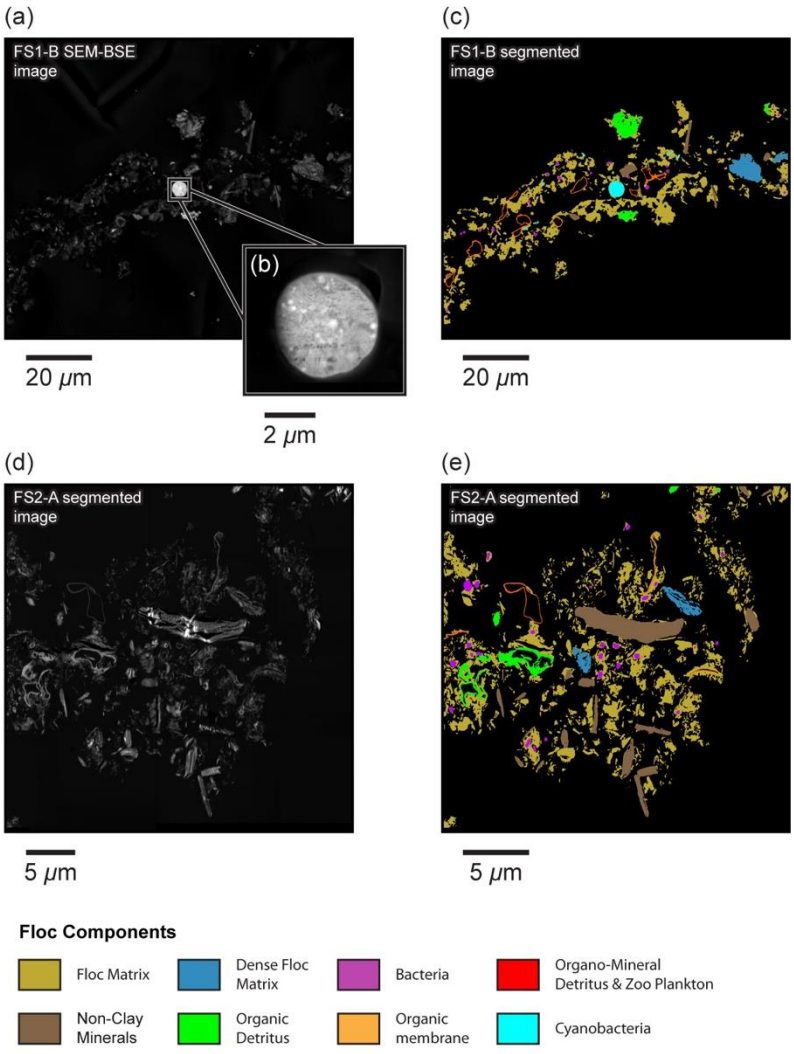

818

819 **Supplementary Fig. S5.** Characterisation of floc sub-micrometre composition and
820 structure in 2D within RoI FS1-B (a) and FS2-A (c). The locations of RoIs FS1-B and
821 FS2-A are shown in Fig. 3c and Fig. S4 of Supplementary Materials respectively. (b)
822 shows a magnified subset from (a) that isolates a single cyanobacteria to
823 demonstrates how differential staining of subcellular structures has taken place.

824

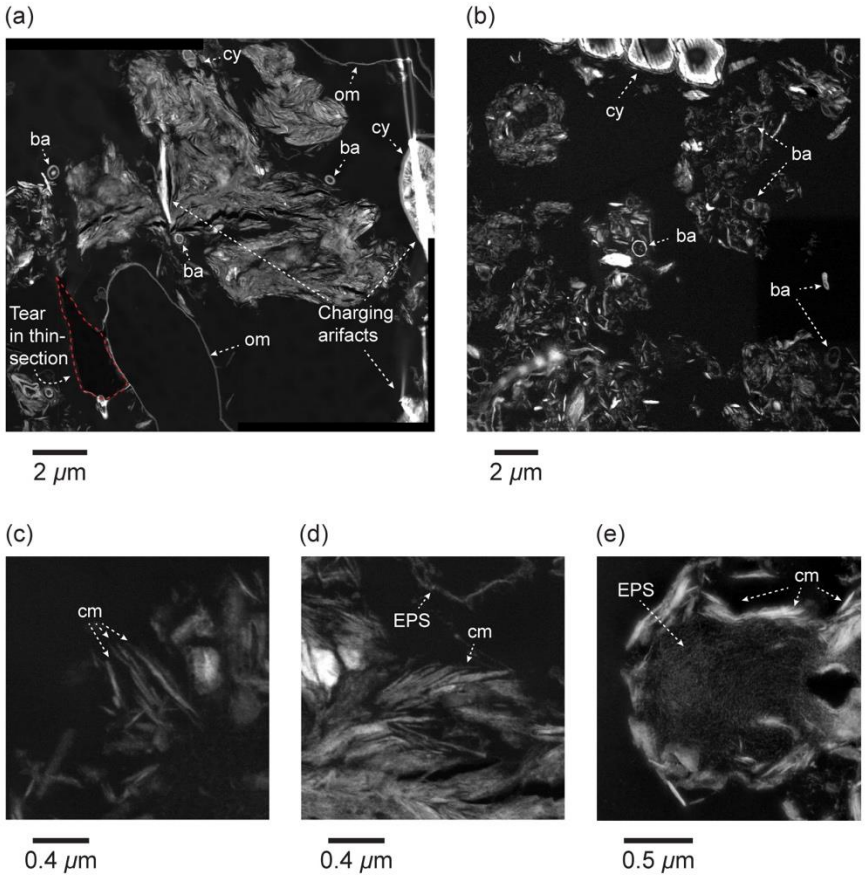

825

826 **Supplementary Fig. S6.** Selected STEM images illustrating the materials and
827 structures commonly observed within flocs FS1 and FS2. Regions of high and low
828 (clay) particle occupation are shown in (a) and (b) respectively. Note that regions of
829 high occupation primarily consisted of clay minerals aligned face-to-face, whereas
830 low occupation regions contained a variety of materials (e.g., clays, decaying organic
831 detritus, bacteria etc.). The high grey-scale values (c. >70) exhibited by units of high
832 occupation likely relates to clays coated in organic material in the nanometre range
833 filling the pore space between clay minerals. Regions of lower occupation were
834 commonly observed to consist of sub-units composed of clay platelets aligned face-
835 to-face and/or edge to face (c-d) and clay minerals arranged around a central
836 bacteria (see Fig. 5a). EPS can be observed filling the nm and μm pores within the
837 floc matrix (e).

838

Declaration of interests

☒ The authors declare that they have no known competing financial interests or personal relationships that could have appeared to influence the work reported in this paper.

☐The authors declare the following financial interests/personal relationships which may be considered as potential competing interests:

The authors declare that they have no competing interests that may have affected the work presented in this paper.